TRUST-AWARE MULTIMODAL DATA FUSION FOR YIELD ESTIMATION: A CASE STUDY OF THE 2020 BEIRUT EXPLOSION

Lekha Patel

Scientific Machine Learning Sandia National Laboratories Albuquerque, NM 87123 lpatel@sandia.gov

Daniel Krofcheck

Complex Systems Risk & Resilience Sandia National Laboratories Albuquerque, NM 87123 djkrofc@sandia.gov

Craig Ulmer

Scalable Modeling & Analysis Sandia National Laboratories Livermore, CA 94550 cdulmer@sandia.gov

Indu Manickam

Complex Systems Risk & Resilience Sandia National Laboratories Albuquerque, NM 87123 imanick@sandia.gov

Jaideep Ray

Computational Data Science Sandia National Laboratories Livermore, CA 94550 jairay@sandia.gov

Stephen J. Verzi

Computational Decision Science Sandia National Laboratories Albuquerque, NM 87123 sjverzi@sandia.gov

Asmeret Naugle

Computational Decision Science Sandia National Laboratories Albuquerque, NM 87123 abier@sandia.gov

November 24, 2025

ABSTRACT

The estimation of explosive yield from heterogeneous observational data presents fundamental challenges in inverse problems, particularly when combining traditional physical measurements with modern artificial intelligence-interpreted modalities. We present a novel Bayesian fractional posterior framework that fuses seismic waves, crater dimensions, synthetic aperture radar imagery, and vision-language model interpreted ground-level images to estimate the yield of the 2020 Beirut explosion. Unlike conventional approaches that may treat data sources equally, our method learns trust weights for each modality through a Dirichlet prior, automatically calibrating the relative information content of disparate observations. Applied to the Beirut explosion, the framework yields an estimate of 0.34–0.48 kt TNT equivalent, representing 12 to 17 percent detonation efficiency relative to the 2.75 kt theoretical maximum from the blast's stored ammonium nitrate. The fractional posterior approach demonstrates superior uncertainty quantification compared to single-modality estimates while providing robustness against systematic biases. This work establishes a principled framework for integrating qualitative assessments with quantitative physical measurements, with applications to explosion monitoring, disaster response, and forensic analysis.

1 Introduction

Explosive yield estimation serves critical functions in international security monitoring, disaster response planning, and forensic accident investigation. For treaty verification under frameworks such as the Comprehensive Nuclear-Test-Ban Treaty, accurate yield determination enables verification of compliance with weapons testing restrictions (Pasyanos and Myers, 2018; Pasyanos and Chiang, 2022). Following industrial accidents involving energetic materials, yield estimates inform emergency response decisions, guide evacuation planning, and support forensic analyses to prevent

future incidents (Pasman et al., 2020; Sadek et al., 2022). In both, timely and accurate yield assessment can mean the difference between effective response and catastrophic outcomes.

Modern disasters generate unprecedented volumes of heterogeneous observational data across multiple sensing modalities. Satellite synthetic aperture radar (SAR) imagery captures spatial damage patterns across entire cities, social media platforms collect thousands of geotagged photographs documenting ground-level structural damage, and seismic networks record body waves and surface waves at regional and teleseismic distances. Recent advances in vision-language models have further enabled automated interpretation of imagery for damage assessment without requiring extensive training datasets (Ahn et al., 2024; Beltre et al., 2025; Gupta et al., 2019). These models can classify structural damage severity from photographs, estimate overpressure from visual cues, and extract quantitative information from unstructured image collections. However, this data proliferation presents both opportunities and challenges. While diverse observations potentially contain complementary information that could reduce yield estimation uncertainty when properly combined, integrating, for example, qualitative visual assessments with quantitative physical measurements requires principled statistical frameworks that account for varying uncertainties and information content across modalities.

Traditionally, yield estimation methods rely on well-calibrated empirical relationships between physical observables and explosive energy. For instance, seismic magnitude scales have been developed through decades of underground nuclear testing (Pasyanos and Ford, 2015; Pasyanos and Kim, 2019), crater dimensions provide direct evidence of energy deposition (Ambrosini and Luccioni, 2006; Holsapple, 1993), and atmospheric infrasound measurements capture acoustic energy propagation (Kim and Pasyanos, 2022). However, each single-modality approach carries substantial systematic uncertainties. Seismic coupling efficiency varies by orders of magnitude depending on geological conditions and emplacement configuration (Khalturin et al., 1998), crater scaling relationships depend critically on substrate properties, moisture content, and burst height (Ambrosini et al., 2002), and atmospheric propagation models require accurate knowledge of temperature and wind profiles that are rarely available in operational settings (Kim and Pasyanos, 2022).

Recent studies have attempted to leverage the complementary information from multiple modalities through joint Bayesian inference. Ford et al. (2021) successfully estimated yield using seismic, acoustic, and optical observations through standard Bayesian inference, demonstrating computational feasibility of multimodal fusion. Kim and Pasyanos (2022) achieved comparable results for the 2020 Beirut explosion using seismoacoustic data with physics-based propagation models, obtaining yield estimates of 0.4–1.4 kt. However, both approaches employ conventional posterior forms $p(\theta|y) \propto p(\theta) \prod_i L(y_i|\theta)$, thus implicitly assuming equal reliability across fundamentally different measurement types. This assumption proves problematic when integrating physics-based forward models with data-driven model outputs. For instance, a seismic measurement in poorly-coupled marine sediments receives the same inferential weight as a direct crater diameter measurement, despite the order-of-magnitude difference in model uncertainty. Similarly, vision-language model (VLM) damage classifications (Krofcheck et al., 2025) that inherently embed perceptual and semantic ambiguities contribute equally to AI-derived overpressure estimates as traditional physical measurements with well-characterized error models. When one modality exhibits systematic bias or model misspecification, this conventional approach lacks mechanisms to down-weight its contribution, allowing corrupted observations to degrade the overall inference. The challenge intensifies when incorporating machine learning interpretations into physics-based inference frameworks, raising fundamental questions regarding how to quantify the reliability of qualitative assessments relative to traditional measurements, how to appropriately weight contributions from disparate data sources, and how to prevent systematic biases in one modality from corrupting overall inference. This motivates our development of learned, data-driven trust weights that automatically calibrate relative modality contributions.

To address this heterogeneity in reliability across modalities, we develop a generalized fractional Bayesian framework in which each data stream contributes a tempered likelihood factor with a learned exponent. Generalized Bayes provides robustness to misspecification through a principled loss-based updating rule (Bissiri et al., 2016), with established schemes for choosing temperature parameters to stabilize inference (Grünwald and Van Ommen, 2017; Holmes and Walker, 2017). We extend this framework to the multimodal setting by placing a Dirichlet prior on modality-specific exponents constrained to the simplex, enabling the data itself to learn relative trust weights while preserving full uncertainty propagation. Rather than assuming equal reliability or manually specifying weights, our approach allows the observations to determine their relative contributions through data-driven calibration that naturally down-weights modalities exhibiting model-data discrepancies whilst amplifying those providing consistent, informative constraints.

1.1 The 2020 Beirut Explosion

The August 4, 2020 explosion at the Port of Beirut provides an ideal test case for multimodal yield estimation. Approximately 2750 tonnes of ammonium nitrate detonated following a warehouse fire, producing 220 fatalities, over 7,000 injuries, and an estimated 15 billion dollars in economic damage (Pasman et al., 2020; Sadek et al., 2022). The

event generated diverse observational data across multiple sensing modalities: regional seismic networks recorded moment magnitude between 3.3 and 3.9, high-resolution satellite imagery documented a 140-meter diameter crater and extensive structural damage extending several kilometers from the detonation point (Pilger et al., 2021), synthetic aperture radar (SAR) interferometry captured coherence loss patterns indicating damage severity, and thousands of geotagged photographs provide ground-level documentation of structural damage.

Previous studies have estimated yields ranging from 0.2 to 1.4 kilotons TNT equivalent using various single-modality approaches (Aouad et al., 2021; Diaz, 2021; Goldstein, 2020, 2021; Kim and Pasyanos, 2022; Pilger et al., 2021; Rigby et al., 2020; Stennett et al., 2020). Table 1 summarizes these estimates and demonstrates substantial variation across methodologies, highlighting the need for integrated multimodal approaches that utilize principled statistical data fusion.

· 1	1. Summary of previous Benefit explosion yield estimates from men						
	Study	Method	Yield (kt TNT)				
Rigby et al. (2020)		Video footage	0.5–1.12				
	Aouad et al. (2021)	Fireball evolution	0.5 - 1.1				
	Diaz (2021)	Image analysis	0.3-0.5				
	Stennett et al. (2020)	Multiple methods	0.5 - 1.1				
	Goldstein (2020, 2021)	Mushroom cloud	0.2 - 0.4				
	Pilger et al. (2021)	Open source data	0.5 - 1.1				
	Kim and Pasyanos (2022)	Infrasound	0.4 - 1.4				

Table 1: Summary of previous Beirut explosion yield estimates from literature

In this paper, we make three novel primary contributions to explosive yield estimation methodology. First, we develop a Bayesian fractional posterior approach with Dirichlet-distributed trust weights that enables principled fusion of heterogeneous data while quantifying the relative information content of each modality. Second, we demonstrate how vision-language model damage assessments can be incorporated into physics-based inference through appropriate forward models and uncertainty propagation, converting qualitative damage classifications into probability distributions over overpressure ranges whilst maintaining full uncertainty quantification. Third, we provide the first unified yield estimate for the Beirut explosion that combines seismic observations, crater measurements, SAR damage patterns, and ground-level image damage assessments.

This paper is organized as follows. In Section 2, we detail the data sources and collection processes. Section 3 presents the hierarchical Bayesian fusion framework. In Section 4, we describe the individual forward models and data utilized for each modality. Section 5 reports empirical yield estimates for each modality separately and the results of the Bayesian data fusion. Finally, Section 6 discusses implications and extensions of our methodology and describes future work.

2 Data Sources

The Beirut explosion generated diverse observational data across multiple sensing modalities. This section describes the data sources employed in the yield estimation framework, with detailed preprocessing procedures provided in the Supplement. The availability of heterogeneous observations spanning traditional physical measurements and modern imagery enables development of robust multimodal fusion methodologies.

2.1 Seismic Waveform Data

We obtained regional seismic waveform data from NSF's Seismological Facility for the Advancement of Geoscience (SAGE). Of 93 stations within a three-degree radius of Beirut, we successfully retrieved one hour of data (15:00–16:00 UTC, August 4, 2020) from 43 stations at epicentral distances of 100–500 km. These stations include all 24 used by the analysis in Pilger et al. (2021), providing comprehensive azimuthal coverage (Figure 1 a). The Python ObsPy library (Beyreuther et al., 2010) was used to extract P-wave and S-wave arrival times, with clear body wave arrivals visible across the regional network (Figure 1 b). The primary challenge for seismic yield estimation is coupling efficiency in Beirut's near-shore environment, where reclaimed land and marine sediments exhibit substantially different mechanical properties than competent bedrock typical of underground nuclear test sites.

2.2 Crater Dimensions from Satellite Imagery

High-resolution satellite imagery captured an elliptical crater at the detonation site, providing direct evidence of explosive energy deposition. We obtained visible-spectrum imagery from two sources: Maxar Technologies (1 m

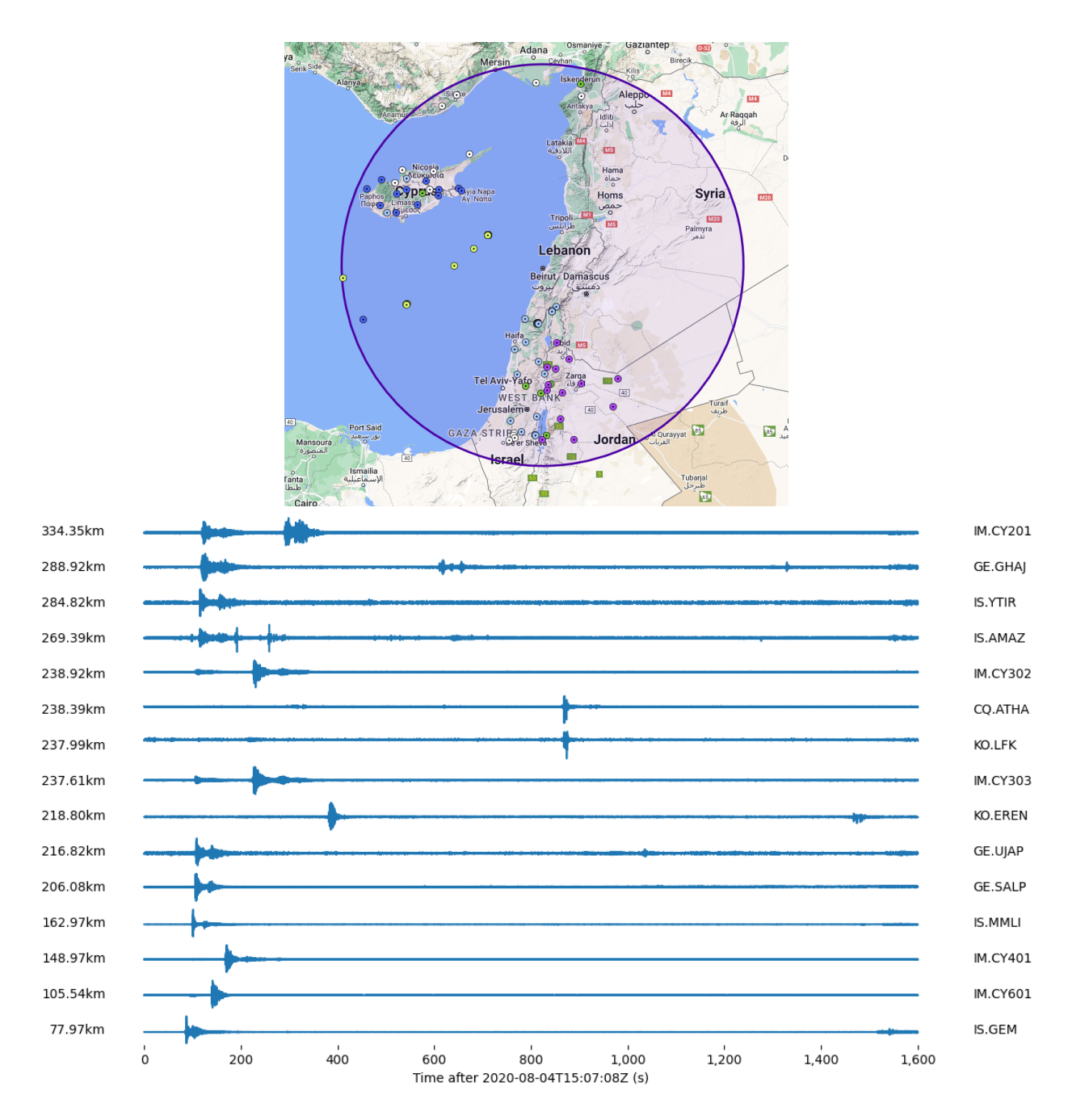


Figure 1: Seismic data from regional stations. Top: Station locations color-coded by distance from epicenter, providing good azimuthal coverage. Bottom: Waveform data sorted by distance, showing clear P-wave and S-wave arrivals with amplitude decay consistent with geometric spreading.

resolution) Maxar Technologies Open Data Program and ESA Sentinel-2 (4 m multispectral). Table S2 summarizes acquisition dates and characteristics. The commercial 1-meter imagery (Figure 2) clearly resolves individual vehicles and structural features, enabling precise crater boundary delineation.

2.3 SAR Coherence Change Detection

SAR (Wikipedia contributors, 2025) coherence analysis quantifies structural damage by measuring decorrelation in repeat-pass acquisitions. We processed four Sentinel-1 acquisition pairs (ascending and descending orbits, July





Figure 2: Resolution comparison for satellite imagery. Individual vehicles are clearly resolved in 1-meter commercial imagery (right), while Sentinel-2 at 4-meter resolution (left) provides adequate large-scale coverage.

30–August 5, 2020) to compute interferometric coherence. Coherence ranges from 1 (no change) to 0 (complete decorrelation), with loss exceeding 0.2 reliably indicating damage (Sudhaus et al., 2021).

2.4 Ground-Level Imagery

Researchers at the American University of Beirut collected 360° photosphere¹ imagery from Beirut's streets a few months after the explosion Sadek et al. (2021a). Anonymized imagery and metadata was subsequently uploaded to the street-image hosting website Mapillary (Mapillary Website), a community website that allows users to store and view planar, 360° panoramic, and 360° photosphere images that are tagged with geotemporal information. We used Mapillary's free API to retrieve 685 photosphere images (238 from August 8–23, 447 from October 1–15) and 4,259 planar images with coordinates (Figure 3a). The photosphere images concentrate in heavily damaged areas and provide omnidirectional coverage including building facades and upper stories. We converted photosphere images to four planar views using oblique viewing angles (10° upward pitch, yaws at 45°, 135°, 225°, 315°) and a resolution of 1600×1200 pixels, and then used vision-language models to identify signs of damage in the images. Visual damage indicators include broken windows with visible glass fragments, debris piles containing masonry and building materials, damaged vehicles, construction barriers marking hazardous structures, and crushed roll-up garage doors (Figure 3b). The primary challenges are temporal delays allowing cleanup efforts (before imaging could be done), spatial sampling gaps, and inferring quantitative overpressure from qualitative visual damage classifications. The Supplement details more of the preprocessing workflow and test suite creation.

The four modalities provide complementary information: seismic waveforms offer established yield-magnitude relationships but suffer from uncertain coupling efficiency (with the ground); crater dimensions provide direct physical evidence with low systematic uncertainty; SAR enables city-wide damage mapping through an indirect overpressure relationship; and ground-level imagery captures detailed damage states but requires converting qualitative assessments to quantitative constraints. The multimodal fusion framework we develop integrates these observations while appropriately accounting for their varying reliability and information content.

3 Theoretical Framework

The estimation of explosive yield from the Beirut explosion presents a classic inverse problem: inferring causal parameters from observed effects. Unlike traditional single-modality inversions, this analysis leverages multiple heterogeneous data sources that observe different physical manifestations of the same event. This section develops the mathematical framework for rigorously combining these disparate observations while accounting for their varying reliability and information content.

¹A photosphere image is a picture that captures views in all directions; see (Vidanapathirana et al., 2019).





Figure 3: Ground-level imagery from Mapillary. (a) Geographic distribution showing photosphere concentration in damaged areas near the port. (b) An example of a ground-level photo with multiple damage indicators (damaged vehicle, broken roll-up garage door, piles of debris, and safety barrier markers). Image from Mapillary.com.

3.1 The Multimodal Inverse Problem

The fundamental task is to estimate the explosive yield $Y \in \mathbb{R}_+$ (in kilotons TNT equivalent) given observations $\mathcal{D} = \{\mathbf{D}_1, \mathbf{D}_2, \dots, \mathbf{D}_M\}$ from M different modalities, where $\mathbf{D}_i \in \mathbb{R}^{n_i}$ and the dimensions $n_i \in \mathbb{N}$ may differ across datasets.

Each dataset \mathbf{D}_i relates to the yield through a forward model that encodes the relevant physics: $\mathbf{D}_i = \mathcal{F}_i(Y; \boldsymbol{\theta}_i) + \boldsymbol{\epsilon}_i$, where $\mathcal{F}_i : \mathbb{R} \to \mathbb{R}^{n_i}$ represents the forward operator mapping yield to expected observations, $\boldsymbol{\theta}_i \in \Theta_i \subseteq \mathbb{R}^{p_i}$ are modality-specific model parameters (such as seismic coupling coefficients, crater scaling exponents, or building fragility curves), and $\boldsymbol{\epsilon}_i \in \mathbb{R}^{n_i}$ represents observation noise. Here, p_i denotes the dimensionality of the parameter space, where in general, $n_i \neq p_i$.

The challenge of multimodal fusion arises because these forward models encode different systematic uncertainties and varying degrees of physical understanding. For instance, seismic coupling can vary by an order of magnitude depending on local geology, crater scaling depends on substrate properties and geometry, and damage assessments require mapping qualitative visual evidence to quantitative overpressure through building vulnerability models. Any principled fusion framework must therefore account for these modality-specific uncertainties without allowing systematic biases in one observation type to corrupt the overall inference.

3.2 Limitations of Conventional Bayesian Fusion

The standard Bayesian approach to multimodal inference assumes conditional independence and treats all observations equally: $p(Y|\mathcal{D}) \propto \pi(Y) \prod_{i=1}^M L(\mathbf{D}_i|Y)$, where $\pi(Y)$ represents prior knowledge about plausible yield values and each likelihood function $L(\mathbf{D}_i|Y)$ quantifies how probable the observations from modality i are given a hypothesized yield. This formulation provides a coherent framework for combining evidence, but it implicitly assumes that all modalities merit equal trust regardless of their information content or model fidelity.

Recent applications have demonstrated both the promise and limitations of this conventional approach. Ford et al. (2021) successfully estimated yield using seismic, acoustic, and optical observations through standard Bayesian inference implemented in Stan, demonstrating computational feasibility and showing that multimodal fusion can reduce uncertainty relative to single-modality estimates. Kim and Pasyanos (2022) achieved comparable results for the Beirut explosion specifically, combining seismoacoustic data with physics-based propagation models to constrain the yield. However, both studies employ the conventional posterior form shown above, which lacks mechanisms to adapt the relative contribution of each modality based on model-data consistency.

Existing general data fusion methodologies offer alternative approaches to combining heterogeneous observations, yet each carries limitations when applied to problems requiring integration of physics-based forward models with

data-driven outputs. Bayesian model averaging provides principled uncertainty quantification by computing posterior probabilities over a discrete set of models and averaging predictions weighted by these probabilities (Hoeting et al., 1999; Fragoso et al., 2018). However, this approach assumes models are exchangeable and typically requires manual specification of prior model probabilities, which may not be reliable for novel data modalities like vision-language model interpretations where validation datasets are limited. The framework also struggles when the set of candidate models does not include the true data-generating mechanism, as is the case when simplified physics-based forward models are employed.

Covariance intersection provides optimal conservative fusion when cross-correlations between estimates are unknown, guaranteeing that fused covariance bounds encompass all possible correlation structures (Julier and Uhlmann, 2007). However, this conservatism significantly degrades performance when estimates are highly correlated, as occurs when multiple modalities observe the same underlying physical quantity through different measurement processes. The method also requires Gaussian assumptions that may be inappropriate for damage observations or other ordinal data. To deal with this, Dempster-Shafer theory explicitly utilizes belief assignments over hypothesis power sets, enabling fusion of uncertain evidence without requiring precise probability distributions (Shafer, 1976), with recent applications to disaster management demonstrating capabilities for handling conflicting information (Fei et al., 2024). Nonetheless, the exponential computational complexity in the number of hypotheses limits scalability, while the framework lacks natural mechanisms for incorporating continuous-valued physics-based forward models.

Additionally, meta-learning approaches enable rapid adaptation to varying sensor configurations by learning optimal fusion strategies from related tasks (Finn et al., 2017), showing promise when sufficient task diversity exists for generalization, which may be hindered for yield estimation due to data sparsity that limits the availability of similar training examples. Nevertheless, all of these methodological limitations share the difficulty in appropriately weighting heterogeneous data sources with fundamentally different noise characteristics, model uncertainties, and information content. To the best of our knowledge, no existing framework systematically addresses this heterogeneity through data-driven reliability quantification while maintaining rigorous uncertainty propagation.

3.3 Fractional Posteriors for Robust Inference

Bayesian fractional posterior methods offer a principled solution to data source heterogeneity through the tempering of likelihood contributions (Wang and Zidek, 2012). Rather than treating all observations equally, the fractional posterior down-weights likelihoods that exhibit poor model-data agreement while amplifying those that provide consistent constraints. The fractional posterior takes the form $p(\theta|x) \propto p(\theta)L(x|\theta)^{\gamma}$, where x denotes the datum, θ the parameter of interest, and $0 < \gamma \le 1$ controls the relative influence of the likelihood versus the prior (Bissiri et al., 2016). When $\gamma = 1$, this reduces to the standard Bayesian posterior, while $\gamma < 1$ reduces the likelihood's influence, making inference more robust to model misspecification. This modification provides robust inference when the assumed model deviates from the true data-generating process. Moreover, Bhattacharya et al. (2019) rigorously established that fractional posteriors achieve posterior contraction rates even under misspecification, proving that the posterior concentrates around the parameter value that minimizes a specific loss function rather than diverging or producing nonsensical inferences.

An important consideration with this framework is temperature parameter selection, which has evolved from ad-hoc choices to principled data-driven approaches through SafeBayes (Grünwald and Van Ommen, 2017) and information-matching (Holmes and Walker, 2017), with recent work demonstrating that appropriate tempering does not impact posterior predictions in moderate-to-large samples (McLatchie et al., 2023). However, these developments address single data sources with one global temperature parameter.

While weighted likelihood methods (Wang and Zidek, 2012) employ modality-specific exponents, these weights are typically fixed a priori or selected through cross-validation requiring substantial validation data. The extension of fractional posterior theory to learn modality-specific exponents through hierarchical Bayesian priors has yet to be explored for multimodal data fusion. This distinction proves critical for explosive yield estimation: when combining seismic measurements with crater dimensions and damage assessments, different modalities warrant different degrees of tempering based on their model fidelity and systematic uncertainties. Our approach enables the data itself to determine these weights while maintaining the theoretical robustness guarantees of fractional posteriors under misspecification.

3.4 Learning Trust Weights Through Hierarchical Modeling

To this end, we formulate multimodal yield estimation via modality-specific exponents that leverages conditional independence between modalities: $p(Y|\mathcal{D}, \gamma) \propto \pi(Y) \prod_{i=1}^M L_i(\mathbf{D}_i|Y)^{\gamma_i}$, where $L_i(\mathbf{D}_i|Y)$ denotes the likelihood for modality i and trust weights $\gamma = (\gamma_1, \ldots, \gamma_M) \in (0, 1]^M$ quantify the relative information content of each modality. The product form assumes conditional independence between modalities given yield, an appropriate assumption since the modalities that we consider observe distinct physical manifestations of damage from different geometries rather than

the same underlying damage state. This hierarchical specification enables data-driven calibration: modalities providing consistent constraints on yield receive higher posterior weights, while those exhibiting model-data discrepancies are naturally down-weighted. The modeling of γ using Dirichlet priors will be discussed in Section 5.1.

4 Forward Models

The success of our multimodal fusion framework depends critically on appropriate construction of forward models \mathcal{F}_i and likelihood functions \mathcal{L}_i for each modality. These components encode both our physical understanding of how yield manifests in observable quantities and the uncertainties inherent in this mapping. This section details the forward model construction, prior specifications, and likelihood formulations for four data modalities: seismic waves, crater dimensions, SAR damage assessment, and vision-language model interpretation of ground-level imagery.

4.1 Overview and Common Elements

The forward models can be categorized into two classes based on their physical directness. Direct measurements such as seismic moment magnitude M_w and crater diameter D, relate to yield through empirical scaling laws established from decades of physical testing. Damage proxies such as the structural damage changes observed in SAR imagery and ground-level photographs, require intermediate modeling that first relates yield to blast overpressure P through blast–propagation models, then connects overpressure to damage states through vulnerability functions.

All modalities share a common prior on yield $\log_{10} Y \sim \text{TruncatedNormal}(\mu = 0.0, \sigma = 0.1, \text{upper} = \log_{10} 2.75)$, where Y is expressed in kilotons TNT equivalent. This prior centers on 1 kt with approximately one order of magnitude uncertainty, truncated at 2.75 kt to reflect the theoretical maximum from complete detonation of the stored ammonium nitrate with TNT-like efficiency and energetic yield.

4.1.1 Blast Overpressure Model: Kingery-Bulmash

Both damage-based modalities (SAR and VLM) require conversion from yield to blast overpressure. Here, we employ the Kingery-Bulmash (KB) correlations (Kingery and Bulmash, 1984) as refined by Swisdak (1994) for hemispherical surface bursts. The incident (side-on) peak overpressure $P_{\rm inc}$ in psi depends on scaled distance $Z=r/W^{1/3}$, where r is range in meters and W is TNT-equivalent mass in kilograms ($W=Y\times 10^6$ kg for Y in kt).

Converting units, we have $Z_{\rm en} = Z_{\rm SI} \times 3.28084/(2.20462)^{1/3} \approx 2.521Z_{\rm SI}$. Here, the subscripts "en" and "SI" stand for English and SI units. The overpressure thereby follows piecewise polynomial expressions in log-space: $\log_{10} P_{\rm inc} = A + B \log Z_{\rm en} + C(\log Z_{\rm en})^2 + D(\log Z_{\rm en})^3 + E(\log Z_{\rm en})^4$, with coefficients specified for three scaled distance regimes (Table S7. This piecewise structure captures distinct physical regimes: strong shock near the detonation point, Mach stem formation at intermediate ranges, and weak shock propagation at large distances. The model provides overpressure in psi, which is, in the following, converted to kiloPascals via $P_{\rm kPa} = P_{\rm psi} \times 6.89476$.

4.2 Seismic Waves

Explosive yield can be inferred from radiated seismic waves through two related source-strength measures. The seismic moment M_0 (N·m or dyne·cm) is a physically grounded scalar quantifying the strength of seismic radiation. For tectonic earthquakes, $M_0 = \mu AD$ where μ is shear modulus, A is fault rupture area, and D is average slip. Here, the moment directly measures the mechanical work performed during shear failure. For explosions, the source mechanism is approximately isotropic rather than shear, and the effective M_0 scales with the pressure-volume work performed on the surrounding medium during cavity expansion. On the other hand, the moment magnitude M_w provides a logarithmic, energy-consistent measure designed to avoid the saturation problems that plague body-wave magnitudes at large sizes: $M_w = \frac{2}{3} \log_{10}(M_0[\text{dyne} - \text{cm}]) - 10.7$. This relationship establishes M_w as an approximately linear function of log-energy across all source sizes. In practice, seismic catalogs report M_w estimated through spectral inversion of regional waveforms, which we employ as the observable in our inference framework.

For surface and near-surface chemical explosions, only a fraction of the explosive energy couples into seismic radiation since the coupling efficiency depends on local geology, water saturation, and confinement geometry. The same explosive yield can therefore produce substantially different moment magnitudes depending on these factors (Khalturin et al., 1998). The Beirut surface burst in a near-shore environment presents particular challenges, as unconsolidated marine sediments exhibit significantly poorer coupling relative to material typical of underground nuclear test sites, which most existing data cover (Pasyanos and Chiang, 2022). This geological variability thus motivates a likelihood formulation with learned variance parameter rather than assuming deterministic yield-magnitude relationships.

In order to define a suitable forward model, we employ a two-stage approach: first, we extract raw seismic waveform features and predict M_w using a 5-member neural network ensemble trained on the dataset of Pasyanos and Chiang (2022) of mixed surface-level chemical and U.S. underground nuclear tests, then we subsequently relate M_w to yield through empirical regression.

The neural network ensemble processes regional seismic waveforms (measured at 100–500 km epicentral distance) to predict $\log_{10} M_0$ directly through five independently trained models with identical architectures but different random initializations. The ensemble prediction is computed as the equally-weighted average: $\log_{10} M_0^{\text{ensemble}} = \frac{1}{5} \sum_{k=1}^{5} \log_{10} M_0^{(k)}$, where $\log_{10} M_0^{(k)}$ is the prediction from the k-th ensemble member. This ensemble approach reduces prediction variance by approximately 40% compared to single-model predictions. Full architectural and training details are provided in the Supplement.

Cross-validation using group 10-fold (ensuring events do not leak between train/test sets) demonstrates that individual ensemble members achieve a mean absolute error of approximately 0.3 orders of magnitude in M_0 prediction, with the ensemble mean further reducing this uncertainty. Figure S2 shows the training history and predictions from a representative ensemble member on a log scale, demonstrating good convergence and alignment between predicted and true values across multiple orders of magnitude spanning the full range of yields in the training dataset. The variance visible in lower- M_0 predictions reflects increased uncertainty for surface chemical explosions compared to buried nuclear tests that dominate the training data. The yield-magnitude relationship subsequently follows an affine transformation on the log scale: $\log Y = \alpha + \beta M_w$, with regression coefficients $\alpha = -14.587$ and $\beta = 3.004$ calibrated from surface-level blasts in Khalturin et al. (1998).

For the observed moment magnitude M_w^{obs} , the expected value given yield Y follows from inversion: $M_w^{\text{pred}}(Y) = \frac{\log Y - \alpha}{\beta}$. We posit a likelihood that assumes Gaussian-distributed residuals: $\mathcal{L}_m(M_w^{\text{obs}}|Y,\sigma_m) = \mathcal{N}(M_w^{\text{obs}}|M_w^{\text{pred}}(Y),\sigma_m^2)$ where the uncertainty parameter σ_m is learned rather than fixed, with prior: $\sigma_m \sim \text{TruncatedNormal}(\mu=0.13,\sigma=0.01,\text{lower}=0.05,\text{upper}=0.30)$. This prior centers on the empirical variance in M_w from the ensemble models, while allowing data-driven refinement to account for differences between the Beirut surface explosion and the underground nuclear tests used for training.

Applied to Beirut, the neural network processes waveforms from regional stations spanning 100–500 km epicentral distance, providing good azimuthal coverage (Figure S3), yielding $M_w = 4.50 \pm 0.13$.

4.3 Crater Geometry

Explosive excavation creates craters whose dimensions scale with yield through dimensional analysis. For gravity-dominated cratering in competent materials, the fundamental relationship relates the crater diameter D to yield, $D \propto Y^{1/3}$, reflecting the volumetric nature of energy deposition (Nordyke, 1961; Schmidt and Housen, 1987).

In logarithmic space, the scaling relationship becomes linear: $\log_{10} D = (\log_{10} Y + 6.0)/3.0$, where D is crater diameter in meters and Y is yield in kilotons (Cooper, 1996). The constant 6.0 reflects unit conversions and average geological conditions for surface bursts.

The Beirut crater exhibits elliptical geometry, reflecting either directional blast effects or substrate anisotropy. Rather than modeling these directional effects explicitly, we treat width and length as independent observations of the idealized circular diameter, acknowledging that both dimensions carry yield information.

The likelihood treats log-transformed dimensions of crater width w and length l, as independent Gaussian observations: $\mathcal{L}_c(w,\ell|Y,\sigma_c) = \prod_{d\in\{w,\ell\}} \mathcal{N}(\log_{10}d|\mu_c(Y),\sigma_c^2)$, where $\mu_c(Y) = (\log_{10}Y+6.0)/3.0$. The uncertainty parameter accounts for both measurement error (satellite resolution, boundary identification) and geological variability: $\sigma_c \sim \text{TruncatedNormal}(\mu=0.08,\sigma=0.02,\text{lower}=0.02,\text{upper}=0.15)$, centering around 0.08 dex (approximately 20% in linear space), consistent with crater scaling studies (Sadek et al., 2022).

Crater dimensions were extracted from Sentinel-2 imagery acquired August 8, 2020, using image segmentation and ellipse fitting techniques; more details are available in the Supplement. An ellipse fitted to the contour yields major axis 108.1 m and minor axis 46.7 m, giving equivalent circular diameter $D_{\rm equiv} = \sqrt{108.1 \times 46.7} \approx 71$ m. Rather than performing separate analyses for the major and minor axes as sensitivity bounds, our Bayesian framework treats both dimensions as independent observations in the likelihood, thereby naturally incorporating the elliptical geometry and directional effects into the yield uncertainty quantification. This measurement closely aligns with independent estimates of 120 m for the major axis (Sadek et al., 2021a). Further details are in Section S2.2.

4.4 Synthetic Aperture Radar Damage Assessment

Interferometric SAR coherence analysis quantifies structural damage by comparing radar backscatter before and after an event. The coherence between acquisitions from identical viewing geometries ranges from 1 (no change) to 0 (complete decorrelation), with loss exceeding 0.2 reliably indicating damage (Sudhaus et al., 2021). We aggregate coherence measurements into 10×10 pixel boxes (approximately $100 \text{ m} \times 100$ m ground footprint) and define the observable $D_{\%,i} \in [0,100]$ as the percentage of pixels flagged as damaged within box i after despeckling and quality filtering.

The forward model $\mathcal{F}_{SAR}(Y; \boldsymbol{\theta}_{SAR})$ relates yield to damage percentage through blast overpressure, employing a learned damage-pressure vulnerability curve to accommodate scene-specific structural heterogeneity.

For each box at distance r_i from the epicenter, we compute incident overpressure using the Kingery-Bulmash correlations (Section 4.1.1): $P_{r,i}(Y) = \mathcal{P}_{\mathrm{KB}}^{\mathrm{inc}}(r_i,Y), P_{\mathrm{kPa},i}(Y) = 6.89476\,P_{r,i}(Y)$. Instead of fixing the damage-pressure relationship through engineering models (Pilger et al., 2021) that may not capture site-specific construction practices, we learn a two-parameter logistic curve in log-pressure space: $\mu_i(Y) = 100\,\sigma\big(K\,[\log_{10}P_{\mathrm{kPa},i}(Y) - \log_{10}P_{50}]\big), \sigma(u) = (1+e^{-u})^{-1}$, where P_{50} (kPa) represents the midpoint overpressure producing 50% expected damage, and K>0 controls the transition gradient. This formulation thus naturally captures the transition from low to high damage while absorbing scene heterogeneity including variations in building age, construction quality, and structural systems into the learned parameters.

SAR observations exhibit heavy-tailed variability from multiple sources: mixed construction within aggregation boxes (the 10×10 pixel boxes with a ground footprint of about 100 meter square), shielding and occlusion effects, registration errors between acquisition pairs, and despeckling artifacts. A Gaussian error model may therefore prove overly sensitive to inevitably large residuals, allowing a few outlier boxes to dominate the likelihood. To deal with this, we instead adopt a Student-t observation model on the logit scale, which naturally accommodates outliers through heavier tails whilst leaving the core fit unchanged when data follow near-Gaussian behavior.

To do so, we define the logit-transformed observations and predictions $y_i \equiv \frac{D_{\%,i}}{100} \in (0,1), z_i \equiv \text{logit}(y_i) = \log(y_i/1-y_i), z_{\mu,i}(Y) \equiv \text{logit}\mu_i(Y)/100$. Further, conditional on yield and curve parameters, we assume: $z_i \mid Y, P_{50}, K, \sigma_{\text{SAR}}, \nu \sim \text{Student-}t \left(\nu, \mu = z_{\mu,i}(Y), \sigma = \sigma_{\text{SAR}}/100\right), \quad \nu > 2$, where ν controls the tail heaviness (smaller ν produces heavier tails; $\nu \to \infty$ recovers Gaussian).

The degrees of freedom parameter is learned from data rather than being fixed, allowing the model to adapt to the actual outlier frequency. The average log-likelihood across retained boxes prevents sample-size dominance in multimodal fusion: $\ell_{\text{SAR}}(Y, P_{50}, K, \sigma_{\text{SAR}}, \nu) = N_{\text{SAR}}^{-1} \sum_{i=1}^{N_{\text{SAR}}} \log \text{Student-}t\left(z_i \mid \nu, z_{\mu,i}(Y), \sigma_{\text{SAR}}/100\right)$.

This formulation incorporates the learned vulnerability curve parameters $\theta_{\rm SAR}=\{P_{50},K,\sigma_{\rm SAR},\nu\}$ into the inference, with broad prior specifications: $P_{50}\sim {\rm LogNormal}(\log 60,0.8), K\sim {\rm HalfNormal}(3),\sigma_{\rm SAR}\sim {\rm TruncatedNormal}(20,10;[5,60]),\nu\sim 2+{\rm Exp}(1/5),$ where the P_{50} prior centers on 60 kPa with broad uncertainty spanning 15–240 kPa (interquartile range), K favors moderate steepness, $\sigma_{\rm SAR}$ accommodates scene heterogeneity, and ν allows data-driven tail behavior with mild preference for heavier-than-Gaussian tails.

The Beirut SAR analysis processes four Sentinel-1 acquisition pairs from ascending and descending orbits spanning July 23 to August 6, 2020. Multiple image pairs provide redundant observations that reduce sensitivity to individual acquisition artifacts, though they introduce registration challenges from slightly different viewing geometries. Since part of this data (4 images) was obtained from Pilger et al. (2021), we addressed the registration challenges by using the 0-point GPS and x-y size of the combined damage image (5th image) in Pilger et al. (2021) to down-sample the 4 separate images. We also collected our own (GRD) data from the Copernicus Browser for all July and August of 2020 (EO Browser, 2020), where each image collected has the exact same 0-point GPS for all four combinations of orientation and relative orbit S1.3. Since the data from Pilger et al. (2021) was already despeckled, we used it as is. We also conducted our own experiments for denoising using a spiking neural network model, SpikeAD (Verzi et al., 2017, 2018a,b), see the Supplementary Materials.

The four individual coherence damage maps were aggregated by summation and normalized by the maximum to keep the composite damage map between 0 and 1, inclusive. Then these pixels were further aggregated into 10×10 windows to produce a finalized damage map (of percentage values between 0 and 100). The resultant composite damage map can be seen in Figure S13 in the Supplement.

4.5 Vision-Language Model Damage Assessment

Ground-level photosphere imagery from Mapillary (see Section 2.4) provides omnidirectional views of building facades and upper stories at hundreds of geotagged locations throughout Beirut. We employ vision-language models (VLMs), specifically Google's gemma-3-27b-it model (Gemma Team, 2025), to classify structural damage severity at each

location, then relate these qualitative assessments to quantitative overpressure estimates through physically-grounded forward models. The vision-language model methodology employed is described in a companion study (Krofcheck et al., 2025), demonstrating the feasibility of VLM-based blast damage assessment through systematic evaluation of three Google Gemma-3 model variants (4B, 12B, 27B parameters) on the Mapillary images from the Beirut explosion. This study establishes the methodological foundation, showing that VLMs can produce probabilistically-calibrated damage classifications with Shannon entropies ranging from 1.43 to 1.82 bits, with the 27B model providing the most confident assessments and superior spatial coherence.

For each image location i, a VLM processes the photosphere (converted to four planar views as described in Section 2.4) and produces a probability mass function $\mathbf{q}_i = (q_{i0}, q_{i1}, \ldots, q_{i8})$ over nine damage categories (and their descriptions) ranging from "None" (category 0) to "Complete Destruction" (category 8), that relate to specific overpressure intervals, following established post-disaster damage assessment scales used in structural engineering (see Table S8 in the Supplement and Lees (2012)). The VLM output represents epistemic uncertainty in damage classification since the model may assign probability mass to multiple adjacent categories when visual evidence is ambiguous. This probabilistic representation proves essential for proper uncertainty propagation, as deterministic classifications would artificially narrow the posterior and fail to account for subjective assessment boundaries.

The forward model $\mathcal{F}_{VLM}(Y;\theta_{VLM})$ relates yield to expected damage classifications through two sequential mappings: yield \rightarrow overpressure via Kingery-Bulmash, then overpressure \rightarrow damage category probabilities via logistic binning, as a result of the VLM's softmax outputs over the 9 damage categories; more details are presented in the Supplement.

For each image at distance r_i from the epicenter, we compute incident peak overpressure (side-on pressure, appropriate for damage to building surfaces) $P_i(Y) = \mathcal{P}_{KB}(r_i,Y), P_{psi,i}(Y)$ in psi. We then map overpressure to a probability distribution over the nine damage categories through logistic binning. We define bin edges in overpressure space: $\mathbf{E}_{psi} = [0.00, 0.04, 0.16, 0.40, 1.10, 2.10, 3.10, 5.10, 10.0, \infty]$ psi, corresponding to engineering thresholds for progressive structural failure (see Table S8). Here, category k nominally corresponds to overpressures in the range $[E_k, E_{k+1})$.

Rather than imposing sharp boundaries that would create artificial discontinuities in the likelihood, we employ soft logistic binning controlled by a spread parameter σ_{dex} (in log-space): $\pi_{ik}(P_i) = \Phi\left(\frac{\log_{10}E_{k+1} - \log_{10}P_i}{\sigma_{\text{dex}}}\right)$

 $\Phi\left(\frac{\log_{10}E_k-\log_{10}P_i}{\sigma_{\text{dex}}}\right)$, where $\Phi(\cdot)$ denotes the logistic cumulative distribution function: $\Phi(x)=1/(1+e^{-x})$. The vector $\pi_i=(\pi_{i0},\ldots,\pi_{i8})$ represents the expected probability distribution over damage categories for a structure at distance r_i experiencing overpressure $P_i(Y)$, with spread σ_{dex} controlling transition sharpness. Larger σ_{dex} produces broader transitions reflecting greater uncertainty in the damage-overpressure relationship from structural variability, whereas smaller values approach deterministic assignment.

This formulation appropriately captures two sources of uncertainty. First, the VLM classification uncertainty (represented by \mathbf{q}_i) reflects perceptual ambiguity in assigning damage categories from visual evidence. Second, the spread parameter σ_{dex} quantifies physical variability in structural response since identical overpressures produce different damage levels depending on building orientation, construction quality, and local shielding effects. Both uncertainties propagate through the forward model into the yield posterior.

The likelihood treats the observed VLM damage PMFs as draws from a multinomial distribution with probabilities determined by the forward model. For image location i, the log-likelihood contribution follows: $\ell_i(Y, \sigma_{\text{dex}}) = \sum_{k=0}^8 q_{ik} \log \pi_{ik}(P_i(Y), \sigma_{\text{dex}})$, representing the cross-entropy between the observed classification distribution \mathbf{q}_i and the model-predicted distribution π_i .

Not all VLM classifications provide equal information. Images with high classification entropy (uniform distributions over many categories) indicate ambiguous damage states that provide weak constraints on overpressure. Conversely, low-entropy classifications (peaked distributions) reflect confident assessments that should receive greater weight. To incorporate this informativeness structure, we apply entropy-based reweighting. This empirical Bayes approach naturally down-weights ambiguous classifications while preserving the full probabilistic structure of the VLM output: $w_i = (1 + H(\mathbf{q}_i))^{-1}, H(\mathbf{q}_i) = -\sum_{k=0}^8 q_{ik} \log_2 q_{ik}, \text{ where } H(\mathbf{q}_i) \text{ denotes the Shannon entropy in bits. We normalize weights by their median and clip to <math>[0.25, 4.0]$ to prevent extreme down-weighting of moderately uncertain classifications while still emphasizing confident assessments. The average log-likelihood across all images subsequently prevents sample-size effects in multimodal fusion: $\ell_{\text{VLM}}(Y, \sigma_{\text{dex}}) = \sum_{i=1}^{N_{\text{VLM}}} w_i \ell_i(Y, \sigma_{\text{dex}}) / \sum_{i=1}^{N_{\text{VLM}}} w_i.$

The spread parameter receives a prior reflecting typical uncertainty in damage-pressure relationships: $\sigma_{\rm dex} \sim {\rm TruncatedNormal}(\mu=0.15,\sigma=0.05,{\rm lower}=0.05,{\rm upper}=0.60)$, centered at 0.15 dex (approximately 40% variability in pressure) with broad support allowing data-driven calibration. Smaller values indicate tight damage-overpressure correlations appropriate for uniform construction, while larger values accommodate heterogeneous building stocks.

The Beirut VLM dataset comprises $N_{\rm VLM}=685$ photosphere images distributed across the city (Figure 3). The VLM identifies damage indicators including broken windows with visible glass fragments, debris piles containing building materials, structural deformation, and facade collapse. As demonstrated in our companion article (Krofcheck et al., 2025), the Google gemma-3-27b-it model achieves consistent damage classification performance with reasonable processing throughput on a single A100. This study confirms that entropy-based weighting successfully identifies ambiguous classifications, with reasonable model agreement across both the 12B and 27B models potentially indicating convergent behavior across model scales.

5 Results

This section presents the yield estimation results obtained through Bayesian inference over the fractional posterior framework.

5.1 Joint Likelihood and Inference Procedure

The joint posterior distribution over yield Y, trust weights $\gamma = (\gamma_{\text{seismic}}, \gamma_{\text{crater}}, \gamma_{\text{SAR}}, \gamma_{\text{VLM}})$, and modality-specific hyperparameters $\theta = \{\theta_{\text{seismic}}, \theta_{\text{crater}}, \theta_{\text{SAR}}, \theta_{\text{VLM}}\}$ is:

$$p(Y, \gamma, \boldsymbol{\theta} | \mathbf{D}) \propto \pi(Y) \pi(\gamma) \prod_{i} \pi(\boldsymbol{\theta}_{i}) \prod_{i} \mathcal{L}_{i}(D_{i} | Y, \boldsymbol{\theta}_{i})^{\gamma_{i}},$$
 (1)

where $\mathbf{D} = \{\mathbf{D}_{\text{seismic}}, \mathbf{D}_{\text{crater}}, \mathbf{D}_{\text{SAR}}, \mathbf{D}_{\text{VLM}}\}$ denotes the complete observational dataset, $\pi(\cdot)$ represents prior distributions, and \mathcal{L}_i denotes the likelihood function for modality i as specified in Section 4. The trust weights are constrained to the simplex through a Dirichlet prior with concentration parameter $\boldsymbol{\alpha} = (\alpha_{\text{seismic}}, \alpha_{\text{crater}}, \alpha_{\text{SAR}}, \alpha_{\text{VLM}})$: $\boldsymbol{\gamma} \sim \text{Dirichlet}(\boldsymbol{\alpha})$, with concentration parameters $\boldsymbol{\alpha} = \mathbf{1}_4$, where $\mathbf{1}_4$ corresponds to the 4-vector of ones, corresponding to a uniform prior over the simplex that expresses no preference for any particular weighting scheme.

The modality-specific hyperparameters comprise: $\theta_{\text{seismic}} = \{\sigma_m\}$ representing seismic magnitude uncertainty; $\theta_{\text{crater}} = \{\sigma_c\}$ capturing crater scaling variability; $\theta_{\text{SAR}} = \{P_{50}, K, \sigma_{\text{SAR}}, \nu\}$ parameterizing the damage-overpressure vulnerability curve, scene heterogeneity, and tail behavior; and $\theta_{\text{VLM}} = \{\sigma_{\text{dex}}\}$ quantifying damage classification uncertainty. Accordingly, the joint inverse problem targets (Y, γ, θ) with effective dimension $1 + 3 + \sum_{i=1}^4 p_i$ (one yield, 3-dimensional simplex-constrained trust weights, and $\sum_i p_i$ modality hyperparameters); in our four-modality case with p = (1, 1, 4, 1) this totals 11 unknowns.

5.1.1 Markov Chain Monte Carlo Sampling

We perform Bayesian inference, sampling from (1) using the No-U-Turn Sampler (NUTS) (Hoffman et al., 2014), an adaptive Hamiltonian Monte Carlo algorithm implemented in Stan (Carpenter et al., 2017). The sampling configuration consists of four independent chains initialized from dispersed starting points, with 8,000 total iterations per chain. The first 2,000 iterations serve as burn-in (warm-up), yielding 6,000 posterior samples per chain for a total of 24,000 samples. We set the target acceptance probability to 0.95 and maximum tree depth to 12 to ensure thorough exploration of the posterior geometry while avoiding divergent transitions.

5.2 Hyperparameter Posteriors

The learned hyperparameters reveal important information about measurement uncertainties and model-data consistency for each modality. Figure S15 in the Supplement displays the posterior distributions for all modality-specific hyperparameters, using the fused data, including the estimated damage to overpressure relationship learned using SAR imagery. The seismic magnitude uncertainty parameter exhibits posterior mean $\sigma_m=0.159$ with 95% highest density interval (HDI) [0.067, 0.245] magnitude units, while the crater scaling uncertainty converges to $\sigma_c=0.080$ with 95% HDI [0.046, 0.121] in \log_{10} -space, corresponding to approximately 20% uncertainty in linear dimensions. The SAR modality learns a damage-overpressure vulnerability curve through four parameters. The 50% posterior mean damage threshold $P_{50}=83.6$ kPa (95% HDI [3.6, 223.3] kPa) suggests that port-area construction exhibited greater blast resistance than typical unreinforced masonry, potentially reflecting reinforced concrete warehouses designed for industrial loads. The transition steepness K=2.16 (95% HDI [0.003, 5.03]) indicates gradual rather than sharp damage thresholds, reflecting heterogeneous structural vulnerability. The scene heterogeneity parameter $\sigma_{\rm SAR}=23.5\%$ (95% HDI [6.3, 39.1]%) quantifies substantial variability not explained by distance alone, potentially encompassing mixed construction, shielding effects, and directional blast patterns. The degrees of freedom parameter $\nu=3.68$ (95% HDI [0.001, 11.4]) indicates notably heavy tails, demonstrating that SAR observations contain significant outliers

requiring robust statistical treatment to prevent distortion of yield inference. The VLM damage classification spread parameter converges to $\sigma_{\rm dex}=0.158$ with 95% HDI [0.066, 0.246] in log-space. The posterior shift from the prior mean of 0.15 reflects both the subjective nature of damage classification and inherent variability in structural response to blast loading, appropriately capturing the challenges of inferring quantitative overpressure from qualitative visual inspection.

The learned hyperparameters demonstrate that the Bayesian framework successfully calibrates modality-specific uncertainties from data while incorporating prior knowledge from physical principles. The tight constraints on crater and seismic uncertainties reflect the maturity of these measurement techniques, while broader SAR and VLM uncertainties acknowledge inherent challenges in damage-based inference.

5.3 Individual Modality Yield Estimates

Before presenting the multimodal fusion results, we examine yield estimates obtained from each modality independently to establish baseline performance and identify systematic trends. Table 2 summarizes the single-modality posteriors, which is also visualized in Figure 4 against the fused posterior.

Table 2: Individual modality yield estimates with posterior statistics							
Modality	Mode (kt)	Mean (kt)	95% HDI (kt)				
Seismic	0.34	0.38	0.41	[0.16, 0.71]			
Crater	0.34	0.43	0.50	[0 11 1 06]			

Crater 0.34 0.43 0.50 [0.11, 1.06] VLM 0.28 0.54 0.71 [0.03, 1.97] SAR 0.26 0.59 0.77 [0.02, 2.08]

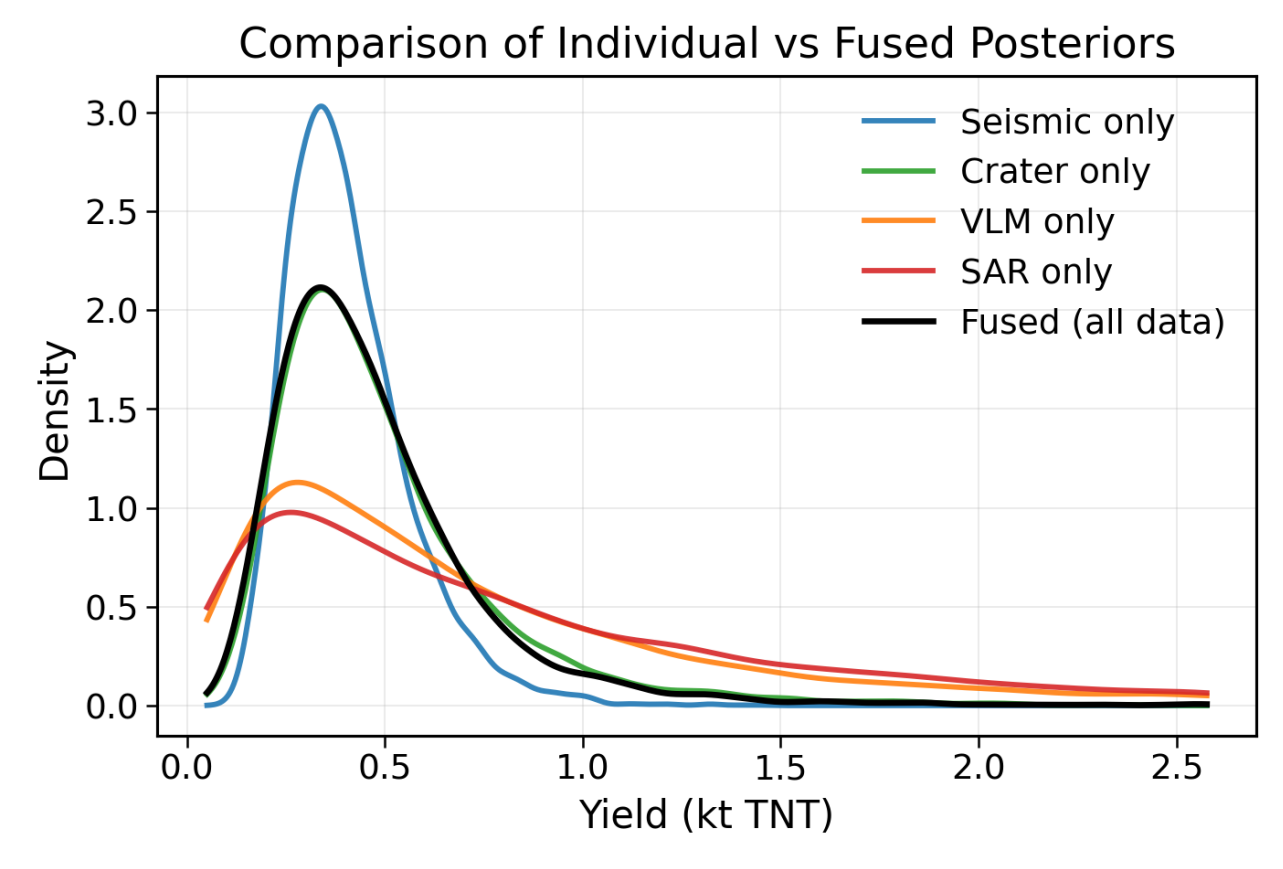


Figure 4: Individual modality posterior distributions for explosive yield against fused posterior.

The seismic and crater modalities demonstrate remarkable convergence with identical modal estimates of 0.34 kt, providing strong independent validation of the explosive yield. The seismic posterior (mode 0.34 kt, 95% HDI [0.16, 0.71] kt) exhibits relatively tight constraints, with the neural network ensemble successfully generalizing

from underground nuclear tests to the surface chemical explosion despite the substantial differences in emplacement conditions. The crater-based posterior (mode 0.34 kt, 95% HDI [0.11, 1.06] kt) provides independent physical confirmation through direct excavation evidence, with broader uncertainty that appropriately accounts for substrate heterogeneity and the observed elliptical crater geometry. The damage-based modalities exhibit substantially greater uncertainty, as expected when vulnerability parameters must be learned jointly with yield from limited observational data. The VLM posterior (mode 0.28 kt, median 0.54 kt, 95% HDI [0.03, 1.97] kt) shows considerable spread, appropriately reflecting the compound uncertainties in mapping qualitative visual damage assessments through overpressure to yield. Similarly, the SAR damage-based posterior (mode 0.26 kt, median 0.59 kt, 95% HDI [0.02, 2.08] kt) exhibits the broadest uncertainty, capturing both the indirect relationship between yield and coherence loss and the epistemic uncertainty from simultaneously learning the vulnerability curve parameters (P_{50} , K, σ_{SAR} , ν).

Despite the heterogeneous uncertainty levels, all four modalities show general consistency with modal estimates clustering in the 0.26–0.34 kt range. The exact agreement between seismic and crater modes is particularly compelling, as these modalities rely on fundamentally different physical processes, yet converge to identical point estimates. The damage-based modalities (VLM and SAR) contribute valuable spatial information covering the entire affected urban area, complementing the point measurements with distributed observations despite their wider posteriors that honestly reflect the combined uncertainties in both yield-to-pressure and pressure-to-damage relationships.

Figure S16 shows the fused posterior for explosive yield obtained by combining all four modalities. The distribution is unimodal with a mild right tail; its center aligns with the 0.34-kt modes of the seismic and crater posteriors in Figure 4, while SAR and VLM contributions broaden the upper tail. We use this fused distribution for all subsequent summaries and validation.

5.4 Learned Trust Weights

The posterior distributions for trust weights reveal the relative information content contributed by each modality. Figure S17 displays the trust weight posteriors. The learned trust weights exhibit posterior mean 0.344 for crater, 0.281 for seismic, 0.221 for VLM, and 0.154 for SAR. Crater observations receive the greatest contribution due to the direct physical relationship between explosive energy and excavation, relatively low systematic uncertainty, and precise satellite-derived measurements. Seismic observations earn substantial weight despite systematic underestimation because the posterior appropriately accounts for geological uncertainty through σ_m , with the tight magnitude measurement ($M_w = 4.50 \pm 0.13$) providing strong constraints. VLM damage assessments contribute moderate weight, demonstrating that qualitative AI-interpreted observations provide useful constraints when uncertainties are properly characterized. SAR receives the lowest contribution due to elevated scene heterogeneity ($\sigma_{\rm SAR} = 23.5\%$), significant outliers requiring heavy-tailed error models ($\nu = 3.68$), and the indirect connection to yield through learned vulnerability curves. The learned damage curve parameters suggest that SAR coherence loss may underestimate structural damage compared to visual assessment, possibly due to radar penetration effects or differing damage mechanisms.

The trust weight posteriors exhibit substantial overlap due to the simplex constraint $\sum_{i=1}^{4} \gamma_i = 1$, with wide credible intervals indicating that multiple weight combinations produce similar posterior yields. This degeneracy reflects that the fused estimate is robust to the precise weighting scheme, with the yield remaining consistent across different weight allocations since all modalities provide complementary constraints.

5.5 Model Validation

To verify that our multimodal fusion framework produces well-calibrated estimates, we performed comprehensive validation through posterior predictive checks and leave-one-out analysis in the Supplement. Posterior predictive checks confirm that data generated from the fitted model closely resemble observed data across all modalities, with p-values near 0.5 indicating absence of systematic bias (seismic: p=0.78, crater: p=0.51). The learned vulnerability curves then successfully reproduce the spatial decay of damage for SAR and VLM observations, with most data points falling within 90% credible intervals. We additionally perform Leave-one-modality-out (LOO) validation which reveals the nuanced relationship between modality agreement and posterior influence. Despite receiving the lowest trust weight, removing SAR produces the largest KL divergence, demonstrating that even down-weighted modalities contribute meaningfully by expanding uncertainty bounds to reflect model disagreement. Crucially, learned trust weights decrease for corrupted modalities, with γ being inversely ranked to LOO KL divergence metrics, confirming that discordant evidence is down-weighted while preserving consensus information.

We additionally perform simulation stress tests that evaluate heavy tails, systematic bias, label noise, cross-modality dependence and other fusion methodologies. Compared with a plain product posterior, a single-temperature model, fixed- γ via cross-validation, Bayesian Model Avergaing (BMA) and covariance intersection, the Dirichlet-tempered

fusion maintains near-nominal 95% coverage with competitive or smaller interval width and lower RMSE under misspecification.

6 Discussion

The fractional Bayesian framework estimates the Beirut explosion yield at 0.34–0.48 kt TNT equivalent (mode-mean, 95% HDI [0.11, 1.00] kt), corresponding to 12–17% detonation efficiency relative to the theoretical maximum of 2.75 kt from complete ammonium nitrate combustion. The incomplete detonation reflects three primary factors characteristic of industrial accidents: unconfined surface burst geometry allowing lateral energy dispersal, heterogeneous storage conditions with variable moisture content and material degradation over years of improper storage, and the large charge diameter exceeding critical dimensions for sustained detonation.

Our central estimate overlaps substantially with the 0.4–1.4 kt range reported by Kim and Pasyanos (2022) and others, validating their seismoacoustic approach while providing tighter constraints through multimodal fusion. The narrower range of our mode-median estimate demonstrates the value of incorporating complementary observations, where crater measurements provide a direct physical anchor and damage-based modalities contribute spatial information across the affected area. The framework successfully reconciles the wide range of literature estimates (Table 1, 0.2–1.4 kt) by revealing that the apparent discrepancy stems from different uncertainty quantification approaches rather than fundamental disagreement.

The success of the fractional fusion approach rests on three critical design decisions that address fundamental challenges in multimodal inference. First, modality-specific tempering through learned trust weights provides an automatic mechanism for handling systematic biases without requiring manual calibration or extensive validation data. The learned weights reveal an informative hierarchy reflecting both physical directness and model-data consistency. Second, the incorporation of vision-language model interpretations demonstrates that qualitative assessments can contribute meaningfully to quantitative inference when properly integrated through physics-based forward models. This represents a methodological advance in bridging the gap between traditional physical measurements and modern AI-interpreted observations. Comprehensive assessment of the VLM damage methodology is presented in Krofcheck et al. (2025), establishing that VLMs can reliably assess blast damage with appropriate uncertainty quantification, though operational deployment requires expert validation datasets as detailed therein. Third, the framework's treatment of conditional independence proves appropriate given the distinct observation geometries of our modalities. SAR and street-level imagery observe fundamentally different physical manifestations of blast effects rather than redundant measurements of the same damage state, supporting the independence assumption. This assumption would break down for modalities with overlapping observation spaces, such as multiple optical satellite images of the same structures, requiring extensions to handle explicit correlation structures.

This work establishes a template for principled integration of heterogeneous observations in explosion monitoring contexts where traditional approaches face limitations. The agreement between our multimodal estimate and previous analyses validates both approaches while demonstrating that fusion can reduce uncertainty without sacrificing accuracy. For treaty verification under the Comprehensive Nuclear-Test-Ban Treaty, the ability to incorporate non-traditional data sources such as commercial satellite imagery and social media could enhance monitoring capabilities, particularly for events where traditional seismic networks provide limited constraints. The framework's robustness to model misspecification, demonstrated through extensive simulation studies, addresses a critical challenge in operational monitoring where forward models are necessarily simplifications of complex physical processes. The learned trust weights provide an interpretable diagnostic for identifying problematic data streams, as evidenced by SAR's low weight correctly flagging model-data discrepancies.

Nevertheless, computational cost of full Bayesian inference may preclude real-time application, though variational approximations or pre-computed surrogate models could address this limitation. Then, the current framework assumes fixed forward models, whereas operational settings might benefit from model selection or averaging over multiple physical models. Future extensions to handle time-series observations and sequential updating as new data arrives would enhance applicability to evolving crisis situations.

Data Availability

Seismic data are available from the Incorporated Research Institutions for Seismology Data Management Center. Satellite imagery from Maxar Technologies and European Space Agency Copernicus program. Ground-level photographs from Mapillary (https://www.mapillary.com). Synthetic aperture radar damage proxy map from Sudhaus et al. (2021) available at https://zenodo.org/records/4762436. Analysis code will be made available upon publication at a Sandia National Laboratories repository.

Author Contributions

L.P. developed the fractional posterior framework, the sesimic methodology and performed the multimodal Bayesian inference. C.U. collected the data, designed the computational infrastructure and vision-language model integration. S.V. and J.R. developed the SAR methodology. I.M. developed the crater methodology. D.K. and A.N. developed the VLM methodology. J.R. conceived the study and provided technical guidance. All authors contributed to manuscript preparation and approved the final version.

Funding

This work was supported by Sandia National Laboratories Laboratory Directed Research and Development program. Sandia National Laboratories is a multimission laboratory managed and operated by National Technology and Engineering Solutions of Sandia, LLC, a wholly owned subsidiary of Honeywell International Inc., for the United States Department of Energy National Nuclear Security Administration under contract DE-NA0003525.

Acknowledgments

This paper describes objective technical results and analysis. Any subjective views or opinions that might be expressed in the paper do not necessarily represent the views of the United States Department of Energy or the United States Government.

References

- Michael E Pasyanos and Stephen C Myers. The coupled location/depth/yield problem for North Korea's declared nuclear tests. *Seismological Research Letters*, 89(6):2059–2067, 2018.
- Michael E Pasyanos and Andrea Chiang. Full moment tensor solutions of US underground nuclear tests for event screening and yield estimation. *Bulletin of the Seismological Society of America*, 112(1):538–552, 2022.
- Hans J Pasman, Charline Fouchier, Sunhwa Park, Noor Quddus, and Delphine Laboureur. Beirut ammonium nitrate explosion: Are not we really learning anything? *Process Safety Progress*, 39(4):e12203, 2020.
- Salah Sadek, Mayssa Dabaghi, Timothy M O'Donnell, Paolo Zimmaro, Youssef MA Hashash, and Jonathan P Stewart. Impacts of 2020 Beirut explosion on port infrastructure and nearby buildings. *Natural Hazards Review*, 23(2): 04022008, 2022.
- Kyeongjin Ahn, Sungwon Han, Sungwon Park, Jihee Kim, Sangyoon Park, and Meeyoung Cha. Generalizable disaster damage assessment via change detection with vision foundation model. *arXiv preprint arXiv:2406.08020*, 2024.
- Angel Beltre, Douglas Crowder, Ritesh Kasamsetty, Jaimie Murdock, Lekha Patel, Salvador Sanchez, Christopher Siefert, Ryan Roche, and Nicholas Winovich. Performance of vision-language models in blast severity analysis. In *Submitted*, 2025.
- Ritwik Gupta, Richard Hosfelt, Sandra Sajeev, Nirav Patel, Bryce Goodman, Jigar Doshi, Eric Heim, Keane Lucas, Howie Choset, and Matthew Gaston. Creating xbd: A dataset for assessing building damage from satellite imagery. In *Proceedings of the IEEE/CVF Conference on Computer Vision and Pattern Recognition Workshops*, pages 10–17, 2019.
- Michael E Pasyanos and Sean R Ford. Determining the source characteristics of explosions near the earth's surface. *Geophysical Research Letters*, 42(10):3786–3792, 2015.
- Michael E Pasyanos and Keehoon Kim. Seismoacoustic analysis of chemical explosions at the Nevada National Security Site. *Journal of Geophysical Research: Solid Earth*, 124(1):908–924, 2019.
- Ricardo Daniel Ambrosini and Bibiana María Luccioni. Craters produced by explosions on the soil surface. *Journal of applied mechanics*, 73(6):890–900, 2006.
- KA Holsapple. The scaling of impact processes in planetary sciences. *Annual Review of Earth and Planetary Sciences*, 21:333–373, 1993.
- Keehoon Kim and Michael E Pasyanos. Yield estimation of the august 2020 Beirut explosion by using physics-based propagation simulations of regional infrasound. *Geophysical Research Letters*, 49(23):e2022GL101118, 2022.
- VI Khalturin, TG Rautian, and PG Richards. A review of nuclear testing by the Soviet Union at Novaya Zemlya, 1955–1990. *Science and Global Security*, 13(1):1–42, 1998.

- RD Ambrosini, BM Luccioni, RF Danesi, JD Riera, and MM Rocha. Size of craters produced by explosive charges on or above the ground surface. *Shock Waves*, 12(1):69–78, 2002.
- Sean R Ford, Douglas S Dreger, Stephen C Myers, and William R Walter. Joint Bayesian inference of explosion yield and height of burst for a historical nuclear test. *Journal of Geophysical Research: Solid Earth*, 126(12): e2021JB022313, 2021.
- Daniel Krofcheck et al. Vision-language models for blast damage assessment: A proof-of-concept probabilistic framework using street-level imagery. *In preparation*, 2025.
- Pier Giovanni Bissiri, Chris C Holmes, and Stephen G Walker. A general framework for updating belief distributions. *Journal of the Royal Statistical Society: Series B (Statistical Methodology)*, 78(5):1103–1130, 2016.
- Peter D Grünwald and Thijs Van Ommen. Inconsistency of Bayesian inference for misspecified linear models, and a proposal for repairing it. *Bayesian Analysis*, 12(4):1069–1103, 2017.
- Chris C Holmes and Stephen G Walker. Assigning a value to a power likelihood in a general Bayesian model. *Biometrika*, 104(2):497–503, 2017.
- C Pilger, P Gaebler, L Ceranna, and T Plenefisch. The 4 august 2020 Beirut explosion: Analysis of the blast using open source information. *Shock Waves*, 31:455–466, 2021.
- CJ Aouad, W Chemissany, P Mazzali, Y Temsah, and A Jahami. Beirut explosion: TNT equivalence from the fireball evolution in the first 170 milliseconds. *Shock Waves*, 31(8):813–827, 2021.
- Jorge S Diaz. Explosion analysis from images: Trinity and Beirut. European Journal of Physics, 42(3):035803, 2021.
- Peter Goldstein. Beirut explosion yield and mushroom cloud height effects of the source environment. Technical report, Lawrence Livermore National Laboratory, 2020.
- Peter Goldstein. Reconciling conflicting estimates of the Beirut explosion yield and mushroom cloud height-effects of an aqueous near source environment. Technical Report LLNL-JRNL-820027, Lawrence Livermore National Laboratory (LLNL), Livermore, CA (United States), 2021.
- Sam E Rigby, TJ Lodge, S Alotaibi, AD Barr, SD Clarke, GS Langdon, and A Tyas. Preliminary yield estimation of the 2020 Beirut explosion using video footage from social media. *Shock Waves*, 30(6):671–675, 2020.
- Chris Stennett, Sally Gaulter, and Jackie Akhavan. An estimate of the TNT-equivalent net explosive quantity (NEQ) of the Beirut port explosion using publicly-available tools and data. *Propellants, Explosives, Pyrotechnics*, 45(11): 1675–1679, 2020.
- Moritz Beyreuther, Robert Barsch, Lion Krischer, Tobias Megies, Yannik Behr, and Joachim Wassermann. Obspy: A python toolbox for seismology. *Seismological Research Letters*, 81(3):530–533, 2010.
- Maxar Technologies Open Data Program. Maxar technologies open data program beirut explosion. https://web.archive.org/web/20250908122945/https://www.maxar.com/open-data/beirut-explosion.
- Wikipedia contributors. Synthetic-aperture radar Wikipedia, the free encyclopedia, 2025.
- Henriette Sudhaus, Andreas Steinberg, and Andre Cahyadi. Damage proxy map inferred from insar and coherence change detection for the Beirut port explosion on august 4, 2021. Available at https://zenodo.org/records/4762436. Accessed: October 23, 2024.
- Madhawa Vidanapathirana, Lakmal Meegahapola, and Indika Perera. Cognitive analysis of 360 degree surround photos, 2019. URL https://arxiv.org/abs/1901.05634.
- Salah Sadek, Mayssa Dabaghi, Paolo Zimmaro, Youssef Hashash, Timothy O'Donnell, and Jonathan Stewart. In person damage assessment and 360° photo collection and analysis, 2021a. URL https://www.designsafe-ci.org/data/browser/public/designsafe.storage.published/PRJ-3030/#detail-2734795894589952491-242ac118-0001-012.
- Mapillary Website. Mapillary. https://www.mapillary.com/. Accessed: 2025-10-31.
- Jennifer A Hoeting, David Madigan, Adrian E Raftery, and Chris T Volinsky. Bayesian model averaging: A tutorial. *Statistical Science*, 14(4):382–401, 1999.
- Tiago M Fragoso, Wesley Bertoli, and Francisco Louzada. Bayesian model averaging: A systematic review and conceptual classification. *International Statistical Review*, 86(1):1–28, 2018.
- Simon J Julier and Jeffrey K Uhlmann. Using exponential mixture models for suboptimal distributed data fusion. *IEEE Aerospace and Electronic Systems Magazine*, 22(11):160–169, 2007.
- Glenn Shafer. A mathematical theory of evidence. Princeton University Press, 1976.

- Liguo Fei, Tao Li, and Weiping Ding. Dempster–shafer theory-based information fusion for natural disaster emergency management: A systematic literature review. *Information Fusion*, 112:102585, 2024.
- Chelsea Finn, Pieter Abbeel, and Sergey Levine. Model-agnostic meta-learning for fast adaptation of deep networks. In *International Conference on Machine Learning*, pages 1126–1135. PMLR, 2017.
- Xinyi Wang and James V Zidek. Data fusion using weighted likelihood. *European Journal of Pure and Applied Mathematics*, 5(1):333–347, 2012.
- Anirban Bhattacharya, Debdeep Pati, and Yun Yang. Bayesian fractional posteriors. *The Annals of Statistics*, 47(1): 39–66, 2019.
- Yuen-Hing McLatchie, Vincent Fortuin, and Aki Vehtari. Robust and scalable Bayesian online changepoint detection. arXiv preprint arXiv:2302.04759, 2023.
- Charles N Kingery and G Bulmash. Airblast parameters from TNT spherical air burst and hemispherical surface burst. Technical Report ARBRL-TR-02555, US Army Ballistic Laboratory, Aberdeen Proving Ground, Maryland, USA, 1984. https://apps.dtic.mil/sti/citations/AD0811673.
- Michael M. Swisdak, Jr. Simplified kingery airblast calculations. Report No. NSWC-TR-5081, 1994. URL https://apps.dtic.gov/sti/citations/ADA526744.
- MD Nordyke. Nuclear craters and preliminary theory of the mechanics of explosive crater formation. Technical Report UCRL-6578, Lawrence Radiation Laboratory, 1961.
- RM Schmidt and KR Housen. Gravity-dominated explosive cratering. *Journal of Geophysical Research*, 92(B7): 5350–5356, 1987.
- P. W. Cooper. Explosives Engineering. Wiley-VCH, New York, 1996.
- EO Browser. Modified copernicus sentinel data 2020/sentinel hub. Sinergise Solutions d.o.o., a Planet Labs company, 2020. URL https://apps.sentinel-hub.com/eo-browser/. Online; accessed March 25 through May 12, 2025.
- Stephen J. Verzi, Craig M. Vineyard, Eric D. Vugrin, Meghan Galiardi, Conrad D. James, and James B. Aimone. Optimization-based computation with spiking neurons. In 2017 International Joint Conference on Neural Networks (IJCNN), pages 2015–2022, 2017. doi:10.1109/IJCNN.2017.7966098.
- Stephen J. Verzi, Craig M. Vineyard, and James B. Aimone. Neural-inspired anomaly detection. In Alfredo J. Morales, Carlos Gershenson, Dan Braha, Ali A. Minai, and Yaneer Bar-Yam, editors, *Unifying Themes in Complex Systems IX*, pages 202–209, Cham, 2018a. Springer International Publishing. ISBN 978-3-319-96661-8.
- Stephen J. Verzi, Fredrick Rothganger, Ojas D. Parekh, Tu-Thach Quach, Nadine E. Miner, Craig M. Vineyard, Conrad D. James, and James B. Aimone. Computing with spikes: The advantage of fine-grained timing. *Neural Computation*, 30(10):2660–2690, 10 2018b. ISSN 0899-7667. doi:10.1162/neco_a_01113. URL https://doi.org/10.1162/neco_a_01113.
- Gemma Team. Gemma 3. Technical report, Kaggle, 2025. URL https://goo.gle/Gemma3Report.
- Frank Lees. Lees' Loss prevention in the process industries: Hazard identification, assessment and control. Butterworth-Heinemann, 2012.
- Matthew D Hoffman, Andrew Gelman, et al. The No-U-Turn sampler: adaptively setting path lengths in Hamiltonian Monte Carlo. *J. Mach. Learn. Res.*, 15(1):1593–1623, 2014.
- Bob Carpenter, Andrew Gelman, Matthew D Hoffman, Daniel Lee, Ben Goodrich, Michael Betancourt, Marcus Brubaker, Jiqiang Guo, Peter Li, and Allen Riddell. Stan: A probabilistic programming language. *Journal of statistical software*, 76:1–32, 2017.
- Salah Sadek, Mayssa Dabaghi, Imad Elhajj, Paolo Zimmaro, Youssef Hashash, Sang-Ho Yun, Timothy O'Donnell, and Jonathan Stewart. Engineering impacts of the august 4, 2020 port of beirut, lebanon explosion. Technical Report GEER-070, Geotechinical Extreme Event Reconnaissance Association, 2021b.
- Fabian Pedregosa, Gaël Varoquaux, Alexandre Gramfort, Vincent Michel, Bertrand Thirion, Olivier Grisel, Mathieu Blondel, Peter Prettenhofer, Ron Weiss, Vincent Dubourg, Jake Vanderplas, Alexandre Passos, David Cournapeau, Matthieu Brucher, Matthieu Perrot, and Édouard Duchesnay. Scikit-learn: Machine learning in Python. *Journal of Machine Learning Research*, 12:2825–2830, 2011.
- Alexander Kirillov, Eric Mintun, Nikhila Ravi, Hanzi Mao, Chloe Rolland, Laura Gustafson, Tete Xiao, Spencer Whitehead, Alexander C. Berg, Wan-Yen Lo, Piotr Dollár, and Ross Girshick. Segment anything. *arXiv* preprint arXiv:2304.02643, 2023.

Andrew Gelman, Xiao-Li Meng, and Hal Stern. Posterior predictive assessment of model fitness via realized discrepancies. *Statistica sinica*, pages 733–760, 1996.

Jonah Gabry, Daniel Simpson, Aki Vehtari, Michael Betancourt, and Andrew Gelman. Visualization in Bayesian workflow. *Journal of the Royal Statistical Society Series A: Statistics in Society*, 182(2):389–402, 2019.

SUPPLEMENTARY MATERIALS

S1 Data Collection and Preprocessing Details

This appendix provides detailed information on data collection procedures, preprocessing workflows, quality assessment, and validation for each modality used in the yield estimation framework.

S1.1 Seismic Data Processing

S1.1.1 Data Retrieval and Storage

Seismic data were retrieved from the Incorporated Research Institutions for Seismology (IRIS) Data Management Center via the SAGE web portal (https://ds.iris.edu/gmap/). Query parameters specified:

- Time window: 2020-08-04T15:00:00Z to 2020-08-04T16:00:00Z
- Geographic radius: 3° from epicenter (33.9016°N, 35.5195°E)
- Network codes: Multiple international networks (IS, GE, IM, CY, etc.)
- Channel preferences: Broadband velocity channels (BH*)

Data were stored in MiniSEED format, with each file named by station code and containing multiple sensor traces (BHE for east-west, BHN for north-south, BHZ for vertical components). Sampling rates ranged from 20–100 Hz depending on station configuration.

S1.1.2 Waveform Analysis with ObsPy

The Python ObsPy library (version 1.4.0) was used for all seismic processing tasks:

Quality Control:

- Gap detection and removal of traces with >5% missing data
- Instrument response correction to ground velocity
- Bandpass filtering (0.5–5.0 Hz) to isolate regional body waves
- Signal-to-noise ratio calculation using pre-event noise window

Phase Picking: P-wave and S-wave arrival times were estimated using the AR-AIC picker with the following parameters:

Window length: 50 samples
Minimum SNR threshold: 3.0
Pick uncertainty: ±0.5 seconds

Manual quality review flagged and excluded poor-quality picks, retaining arrivals with clear onset times.

S1.1.3 Station Metadata

Table S1 summarizes key characteristics of the 43 stations used in the analysis.

Table S1: Regional seismic station characteristics

Distance Range (km)	Count	Azimuth Coverage	Avg SNR
100–200	12	45°-315°	18.5
200-300	18	15°-340°	12.3
300–400	10	30°-290°	8.7
400–500	3	75°–210°	6.2

The station distribution provides good azimuthal coverage with slight gaps in the southwestern quadrant. Distance-dependent amplitude decay follows theoretical geometric spreading (r^{-1}) and anelastic attenuation models for the Eastern Mediterranean crustal structure.

S1.2 Crater Measurement Methodology

Table S2 summarizes imagery acquisition dates and characteristics for visualizing the crater left by the blast.

Table S2: Summary of satellite imagery sources

Source	Before	After	Type	Resolution
Maxar Technologies	2	1	Color	1 m
ESA Sentinel-1	21	17	SAR	20 m
ESA Sentinel-2	5	5	Color	4 m
ICEYE	3	4	SAR	1 m

S1.2.1 Image Selection and Preprocessing

Crater dimensions were extracted from Sentinel-2 Level-2A imagery (surface reflectance product) acquired August 8, 2020, at 08:21 UTC. This acquisition provided:

- Cloud-free coverage of the port area
- 10-meter resolution in RGB bands
- Georeferencing accuracy <10 meters
- Near-nadir viewing geometry minimizing distortion

Images were reprojected from UTM Zone 36N (EPSG:32636) to a local Transverse Mercator projection centered on the explosion site to minimize area distortion for linear distance measurements.

S1.2.2 Automated Boundary Detection

Meta's Segment Anything Model (SAM) was applied to detect the crater boundary through the following workflow:

Water Color Detection:

- 1. Compute normalized difference water index: NDWI = (Green NIR)/(Green + NIR)
- 2. Apply threshold NDWI > 0.3 to isolate water pixels
- 3. Apply SAM with point prompts at visually identified crater edges
- 4. Extract contour from SAM's highest-confidence mask

Ellipse Fitting: Least-squares ellipse fitting to the extracted contour yielded:

- Major axis: 108.1 ± 5.2 m (uncertainty from SAM mask confidence)
- Minor axis: $46.7 \pm 3.8 \text{ m}$
- Orientation: 72° from north (aligned with warehouse long axis)
- Equivalent circular diameter: $D_{\rm equiv} = \sqrt{108.1 \times 46.7} = 71.0~{\rm m}$

Validation: Manual measurements using QGIS polygon tools on the same imagery yielded $106.3 \text{ m} \times 48.1 \text{ m}$, confirming SAM's automated extraction within measurement uncertainty. Independent estimates from the PRJ-3030 GEER report cite major axis 120 m based on field surveys and different imagery sources.

S1.3 SAR Processing Workflow

S1.3.1 Acquisition Pairs and Processing

Four Sentinel-1 Interferometric Wide Swath (IW) acquisition pairs were processed:

Standard InSAR Processing:

- 1. Co-registration: Sub-pixel alignment using cross-correlation
- 2. Interferogram formation: Complex multiplication of master × conjugate(slave)

Table S3: Sentinel-1 acquisition pairs for coherence analysis

Orbit	Dates	Baseline (m)	Mean Coherence
Ascending 1	Jul 30 / Aug 5	45	0.68
Ascending 2	Aug 1 / Aug 7	52	0.65
Descending 1	Jul 31 / Aug 6	38	0.71
Descending 2	Aug 2 / Aug 8	61	0.62

- 3. Coherence estimation: 10×10 pixel sliding window
- 4. Geocoding: Map to ground coordinates using SRTM DEM
- 5. Threshold: Coherence loss >0.2 flagged as damaged
- 6. Compositing: Logical OR across all pairs (pixel damaged if any pair shows loss)

S1.3.2 SpikeAD Despeckling

Standard median filtering modifies all pixels uniformly, potentially blurring damage boundaries. SpikeAD (Spiking Adaptive Despeckling) selectively modifies only outlier pixels using median absolute deviation from the median (or MAD) computed values:

Algorithm:

- 1. For each pixel, compute local median and MAD in 11×11 window
- 2. If $|pixel median| > 3.0 \times MAD$, replace with weighted median
- 3. Otherwise, retain original value
- 4. Iterate 4 times for aggressive noise reduction

This adaptive approach preserves contiguous damage regions while removing isolated speckle noise. Figure S5 demonstrates effectiveness on the August 5 acquisition.

S1.3.3 Zonal Aggregation

To focus on locations experiencing near-direct blast exposure:

- 1. Aggregate damage into 10×10 pixel boxes ($100 \text{ m} \times 100 \text{ m}$)
- 2. Compute damage percentage per box (fraction of pixels flagged)
- 3. Partition city into 15 concentric annuli (radii 200 m to 8 km)
- 4. Within each annulus, retain only 95th percentile boxes
- 5. Final dataset: 150–200 boxes distributed across distance ranges

This zonal thresholding addresses the challenge that tall structures in line-of-sight experience maximum damage while surrounding areas show lower damage from shielding and reflected waves. By selecting high-percentile boxes, we focus on locations where simplified Kingery-Bulmash models are most applicable.

S1.4 Ground-Level Image Processing

Mapillary is a commercial website that hosts community-supplied, street-level images of cities from around the world. Shortly after the 2020 Beirut explosion, Mapillary users posted geo-tagged pictures from cell phones, dashboard cameras, and 360° photosphere cameras. Most notably, researchers from the American University of Beirut (AUB) Maroun Semaan Faculty of Engineering and Architecture (MSFEA) uploaded 2,100 photosphere images taken during a building survey that took place two months after the event. As documented in section 4.2 of the NSF-sponsored Geotechnical Extreme Event Reconnaissance (GEER) report Sadek et al. (2021b), the AUB researchers attached a GoPro Fusion camera to the roof of a vehicle and collected geotagged, photosphere images as they systematically drove through the streets of the city near the port. The resulting images were uploaded to Mapillary for public hosting. Mapillary blurs faces and license plates to mitigate privacy concerns and allows users to access content through a website and a free API.

S1.4.1 Mapillary API Queries

We obtained an API toked from Mapillary and used v4 of the Mapillary Graph API to obtain metadata for images that were taken in the Beirut area from August to the end of December in 2020. Our initial query to retrieve metadata for 2,000 images is as follows:

An examination of the initial set of metadata revealed that multiple users had contributed images besides the AUB MSFEA researchers. Additional metadata queries were placed to determine the number of planar and photosphere images available for each users. Images with incomplete position information (i.e., empty "computed_geometry" fields) were excluded from consideration. As listed in Table S4, a large number of photosphere images were available from chadifa and aubmsfea.

Table 51. Ground level image counts from different Mapmary asers						
User	Dates	Planar	Planar Photosphere			
aubmsfea	Oct 01 – Oct 15	0	1,867	447		
chadifa	Aug 08 – Aug 23	136	884	238		
mohamadmaktabi	Aug 09 – Aug 12	976	0	229		
patsy	Aug 04 – Aug 12	268	0	57		
talamoukaddem	Aug 08	50	0	7		
ziadg	Oct 10 – Nov 19	4,425	0	3,966		

Table S4: Ground-level image counts from different Mapillary users

We retrieved a total of 4,944 images from the list of 8,606 images that had valid position information.

S1.4.2 Photosphere Planarization

We observed two kinds of photosphere formats in the downloaded Mapillary dataset: equirectangular images from user aubmsfea and dual hemisphere images from user chadifa. Anticipating that the warping found in these formats might impede image analysis algorithms, we used the 360-to-planer-images library² to extract four planar images from each photosphere image. Initial work extracted planar images at cardinal yaws (0°, 90°, 180°, 270°) and a 30° pitch. Unfortunately, these perspectives were found to be problematic for the task of analyzing building structures and were therefore discarded. The primary concerns were that the forwards and backwards views focused more on the streets than buildings, the left and right views hit camera blind spots in the dual-hemisphere images, and the 30° pitch was frequently too high to observe ground floor details.

The second and final set of planar image extractions shifted the yaws by 45° (45° , 135° , 225° , 315°) and decreased the pitch to 10° . Each planar image was rendered at 1600×1200 pixels to enable fine detail resolution. These adjustments improved visibility of the nearby buildings. Figure S1 provides an example of how an equirectangular image with a damaged warehouse is split into four planar views. While the warehouse in the original image is split between the left and right edges of the equirectangular image, the front-right and back-right planar images present contiguous views that can be processed more easily by image analysis algorithms.

S1.4.3 Damage Indicator Catalog

We manually inspected approximately 100 random images from the Mapillary dataset to gain a sense of what could be observed in the pictures and generate a list of features that could reliably serve as damage indicators for this situation. We determined that there are multiple confounding factors in this work. First, many of the buildings in the region have pre-existing damage from decades of regional conflict. Mapillary did not have enough images available from before the blast to determine whether damage was old or new. Second, most images were captured a few weeks to a few months after the blast. The impact of this delay is that several common damage indicators (e.g., smoke, fires, emergency workers, human casualties, etc.) are not present in the image, but signs of longer-term cleanup operations (e.g., piles

²https://github.com/Maxiviper117/360-to-planer-images



Figure S1: An equirectangular photosphere image planarized into four views. Views to the left depict no damage, while views to the right include significant damage to a sheet metal warehouse. All images were provided by Mapillary.com.

of debris, construction, safety barriers, etc.) are visible. Third, many buildings have open windows due to the warm climate, making it difficult for vision algorithms to correctly discern between open and broken windows. Finally, Beirut has routine construction that is unrelated to the blast.

We selected the items listed in Table S5 to serve as our key damage indicators when analyzing images. Given the confounding factors of the observations, damage assessments require multiple concurrent indicators rather than relying on single features. The situational limitations necessitate robust uncertainty quantification when converting visual damage classifications to quantitative overpressure estimates, as addressed through the learned spread parameter σ_{dex} in the Bayesian framework.

Table S5: Identified damage indicators and reliability

Indicator	Reliability Notes
Broken windows with visible glass	High reliability; distinguish from open windows
Debris piles with masonry/glass	Moderate; requires distinguishing from routine garbage
Damaged vehicles (crushed roofs)	High reliability; exclude general disrepair
Construction barriers/safety tape	High reliability when outside damaged structures
Crushed roll-up garage doors	High reliability; specific to blast overpressure
Boarded-up storefronts	Moderate; may predate blast in conflict-affected areas
Missing/collapsed walls	Very high reliability; unambiguous structural failure
Displaced building materials	High reliability when coupled with other indicators

S1.4.4 Test Suite Composition

We assembled four test suites of images to support our evaluation of how well vision LLMs could assess damage from images:

Suite 1: Positive Damage Examples (23 images) For the first suite we hand selected 23 images from the Mapillary dataset that provide clear examples of each type of damage indicator. Each image was labeled with 18 different visual indicators of damage (e.g., broken window, missing wall, pile of ruble, damaged car, construction barrier, etc). These images and labels were used for precision and recall assessment.

Suite 2: Negative Damage Examples (25 images) The second suite of examples selected 25 images of cities without visible signs of damage, including Beirut (pre-blast), New York City, and Albuquerque. These images were used to assess false positive rates.

Suite 3: Distributed Spatial Sampling (120 images) To address concerns that the Beirut Mapillary image locations were not evenly distributed, we partitioned the city into a 500 m x 500 m grid and picked a random sample from each grid cell for the third suite of examples. This sampling ensures representative geographic coverage.

Suite 4: GEER Ground-Truth Locations (616 planar views) The dataset associated with the GEER report (Sadek et al., 2021b) includes a list of 154 structural assessments that were made for buildings in the city after the blast. Our fourth test suite selects the photosphere image that is closest to each assessment and uses its four planar images to represent the location. This suite enables expert-generated labels to be associated with images.

S1.5 Metadata Tables

S1.5.1 Mapillary Image Metadata

We constructed a single Parquet file to hold all the metadata associated with the Mapillary images that have valid location information. The majority of the metadata fields are identical to those retrieved from Mapillary's metadata API. The fields are summarized in Table S6.

Field Description **Type** id String Unique ID assigned by Mapillary (alphanu-Track identifier for images from one upload sequence String session computed_geometry **GeoJSON** Point geometry with longitude/latitude in WGS84 computed_compass_angle Float Camera heading in degrees (0–360, clockwise from north) Altitude estimate in meters above sea level computed altitude Float captured_at ISO DateTime UTC timestamp when image was originally captured Username and numeric user ID of image creator Object contributor True if 360° photosphere, False if planar is pano Boolean URL Link to 320px thumbnail on Mapillary thumb_original_url **CDN** Float Extracted from computed_geometry for Longitude convenience Latitude Float Extracted from computed_geometry for convenience Username String Extracted from creator object Local filesystem path to downloaded full-File Path resolution image Computed haversine distance to explosion Distance m Float epicenter

Table S6: Complete metadata fields for Mapillary images

S1.6 Data Attribution and Availability

Seismic Data: Available from IRIS Data Management Center (http://ds.iris.edu/) under open data policies of contributing networks.

Satellite Imagery:

- Maxar/Digital Globe: Open Data Program (https://www.maxar.com/open-data)
- Sentinel-1/2: Copernicus Open Access Hub (https://scihub.copernicus.eu/)
- ICEYE: Commercial license (contact for access)

SAR Damage Proxy Map: Sudhaus et al. dataset available at Zenodo (https://zenodo.org/records/4762436) under CC BY 4.0 license Sudhaus et al. (2021).

Ground Imagery: Mapillary platform (https://www.mapillary.com) requires attribution in publications. We gratefully acknowledge Mapillary and the American University of Beirut researchers for making this data publicly available.

Code and Processed Data: Analysis code and intermediate data products will be deposited in a Sandia National Laboratories repository upon publication, with DOI assignment for reproducibility.

S2 Additional Information on Forward Models

Table S7: Kingery-Bulmash coefficients for incident overpressure (hemispherical surface burst). The numerical values are reproduced from (Swisdak, 1994).

$Z_{\rm en}$ Range (ft/lb ^{1/3})	A	B	C	D	E
[0.5, 7.25) [7.25, 60.0) [60.0, 500.0]	6.914 8.831 5.424	-1.439 -3.700 -1.407	-0.282 0.271 0	$ \begin{array}{c} -0.142 \\ 0.073 \\ 0 \end{array} $	$0.069 \\ -0.013 \\ 0$

S2.1 Seismic Neural Network Architecture and Feature Engineering

Feature Extraction from Regional Waveforms

We extract 250 physics-motivated features from raw seismic waveforms recorded at regional distances (100–500 km). The feature extraction preserves absolute amplitude information critical for yield estimation, as seismic moment scales directly with explosive energy. From each waveform, we compute features across multiple domains:

Time-Domain Features We extract peak amplitude statistics including the absolute maximum amplitude on the \log_{10} scale ($\log_{10} |x_{\rm max}|$), which serves as the primary amplitude scaling factor. Additional metrics include mean, standard deviation, skewness, kurtosis, and the 95th and 99th percentiles of absolute amplitudes. The time of maximum amplitude (normalized by trace length) captures the relative arrival timing of peak energy.

P-Wave Band Features A 0.5–5 Hz Butterworth bandpass filter isolates regional P-waves, from which we compute the filtered maximum amplitude, RMS energy, and ratio to unfiltered maximum. The P-wave energy on the \log_{10} scale $(\log_{10} \sum x_p^2)$ provides a band-limited energy measure less sensitive to noise than broadband measurements.

Frequency-Domain Features The power spectral density is computed via FFT, from which we extract the dominant frequency, spectral centroid, and power distribution across four bands: 0.1-0.5 Hz (very low), 0.5-1.0 Hz (low P-wave), 1.0-5.0 Hz (standard P-wave), and 5.0-10.0 Hz (high frequency). Each band contributes both absolute power (\log_{10} scale) and relative power (fraction of total).

Coda Features We separate P-wave and coda windows, with the P-wave window extending 5 seconds or 30% of the trace length (whichever is smaller), and coda beginning 2 seconds after the P-wave window. The P-to-coda amplitude ratio on the log scale captures the partitioning between body and scattered wave energy. Coda decay rate is estimated via linear regression in log-envelope space, providing a measure of attenuation.

Envelope Features The Hilbert transform provides the analytic signal envelope, from which we extract maximum, mean, and standard deviation. Signal duration is defined as the time span where the envelope exceeds 10% of its maximum. Energy distribution metrics (t_{50} and t_{90}) quantify the temporal concentration of seismic energy.

S2.1.1 Neural Network Architecture

After removing constant features (standard deviation $< 10^{-6}$), we retain 46 informative features that exhibit variance across the dataset. The neural network employs a fully-connected architecture with four hidden layers of dimensions [512, 256, 128, 64], incorporating batch normalization after each linear transformation and ReLU activations. Dropout with rate 0.3 is applied between layers for regularization.

The network is physics-informed through a dual-head architecture: the primary head predicts $\log_{10}(M_0)$ directly, while an auxiliary head predicts moment magnitude M_w . During training, we enforce the physical constraint $M_w = \frac{2}{3}\log_{10}(M_0) - 6.07$ (for M_0 in N·m) through a composite loss function:

$$\mathcal{L} = \mathcal{L}_{\text{data}}(\log_{10} M_0^{\text{pred}}, \log_{10} M_0^{\text{true}}) + 0.1 \mathcal{L}_{\text{physics}}(M_w^{\text{pred}}, M_w^{\text{physics}})$$
 (S1)

where $M_w^{\text{physics}} = \frac{2}{3} \log_{10} M_0^{\text{true}} - 6.07$ ensures physically consistent predictions.

S2.1.2 Ensemble Training for Variance Reduction

To reduce prediction uncertainty inherent in single neural networks, we train an ensemble of five models with identical architectures but different random initialization seeds. Each model is trained on the complete dataset rather than bootstrap samples, allowing all models access to the full training distribution while maintaining diversity through different weight initializations and stochastic gradient descent trajectories.

The ensemble prediction for the Beirut explosion yields $\log_{10}(M_0) = 15.85 \pm 0.20$ (N·m), corresponding to $M_w = 4.50 \pm 0.13$. The standard deviation across ensemble members (0.20 in \log_{10} space) represents approximately 60% relative uncertainty in linear M_0 , substantially lower than single-model predictions which exhibit standard deviations of 0.3–0.4 in \log_{10} space.

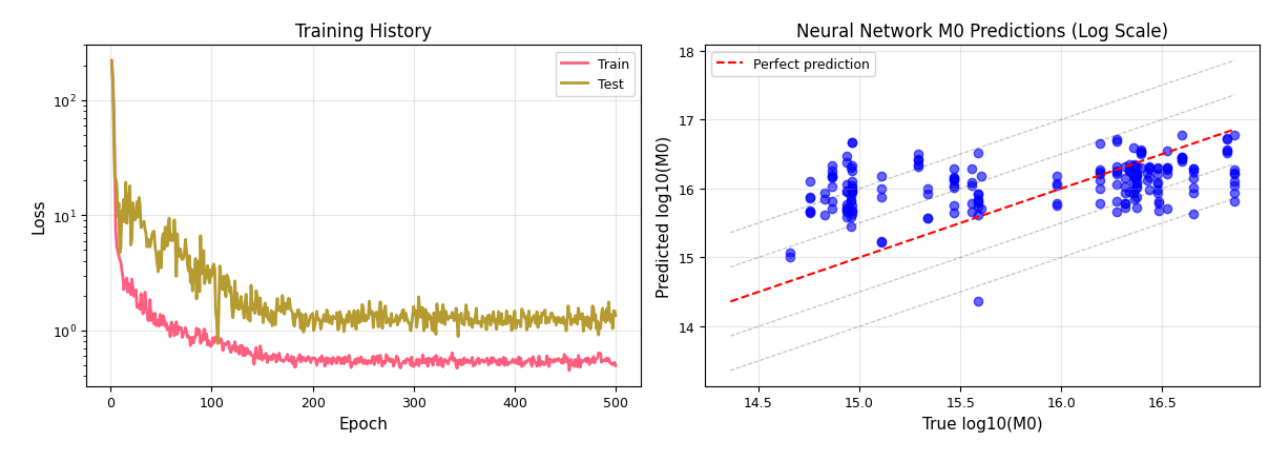


Figure S2: Neural network ensemble member performance for seismic yield estimation. (a) Training history showing loss convergence over 500 epochs for both training and test sets from a representative model, demonstrating effective learning without overfitting. (b) Predicted versus true $\log_{10}(M_0)$ values from a single ensemble member showing good agreement across the full range of seismic moments in the training dataset. The dashed red line indicates perfect prediction.

S2.1.3 Training Configuration

The model is trained using the Adam optimizer with learning rate 10^{-3} and gradient clipping at norm 1.0. We employ GroupKFold cross-validation (Pedregosa et al., 2011) during model development to prevent data leakage, ensuring events from the same explosion do not appear in both training and validation sets. Feature scaling uses RobustScaler (Pedregosa et al., 2011) to handle outliers common in seismic data. Each ensemble member trains for 250 epochs with batch size 32, using early stopping based on validation loss with patience of 40 epochs.

Cross-validation on the mixed chemical/nuclear test dataset yields a mean absolute error of 0.30 orders of magnitude in M_0 prediction (90th percentile error: 0.45 orders). The model exhibits some systematic bias for surface chemical explosions, with correlation between key features and $\log_{10}(M_0)$ remaining moderate (e.g., absolute amplitude: r=0.52, coda decay rate: r=0.14), reflecting the challenge of generalizing from underground nuclear tests to surface chemical explosions.

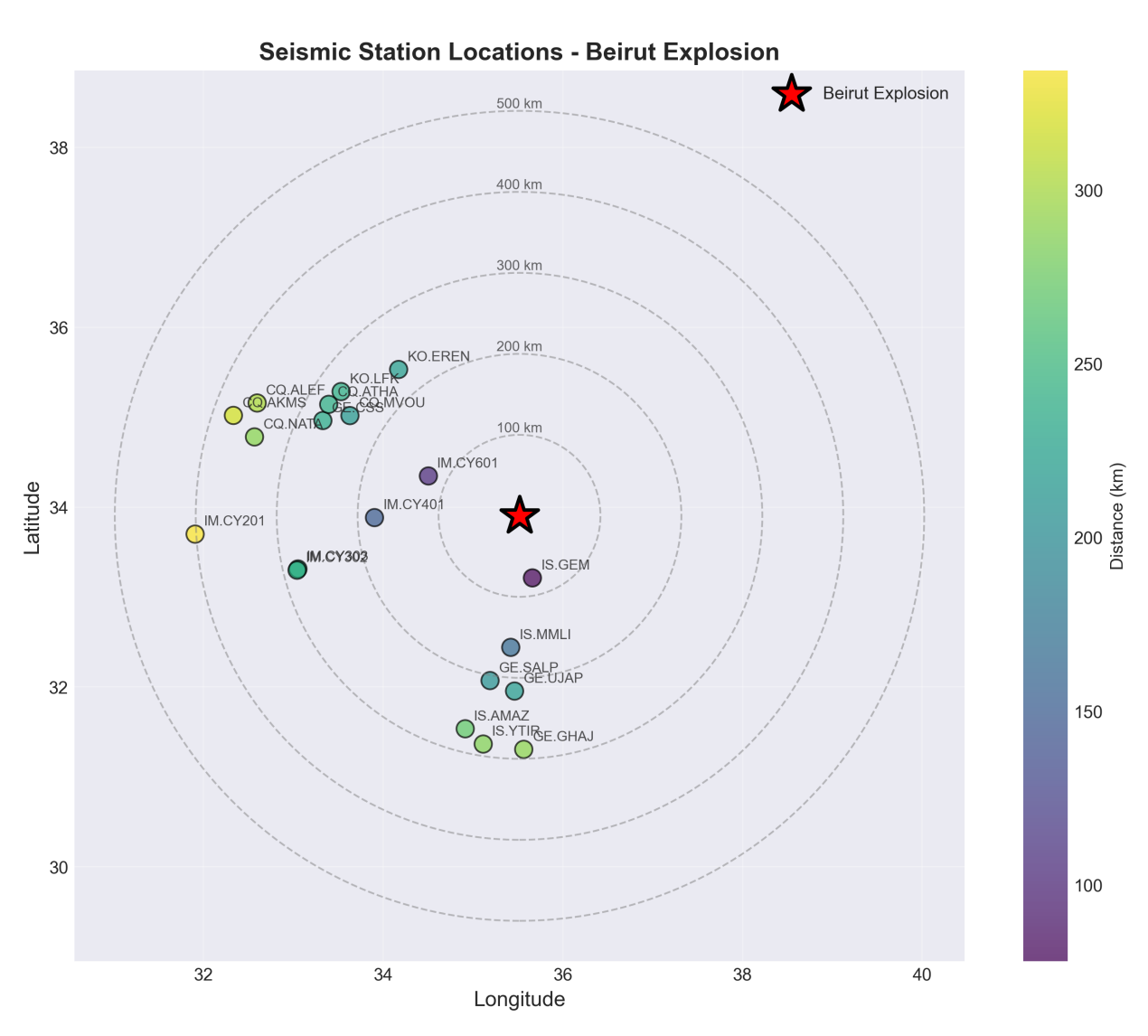


Figure S3: Regional seismic station locations for Beirut analysis. Red star marks the explosion epicenter; circles show 100 km distance intervals. Station colors indicate distance from epicenter, with networks (IS: International Monitoring System, GE: GEOFON, IM: Cyprus) providing comprehensive azimuthal coverage.

S2.2 Crater Geometry

The crater was estimated as an ellipse with dimensions of 46.7 meters in width and 108.1 meters in length, with an aspect ratio of 2.3. The significant departure from circular geometry is likely due to the warehouse geometry and directional effects from the ammonium nitrate storage geometry.

The crater geometry was estimated based on a post-Sentinel-2 colored satellite image capturing the blast region on August 8, 2020. The outline of the crater was estimated based on visible features indicating the blast line using Meta's Segment Anything Model (SAM) (Kirillov et al., 2023) with a user specified reference point at the center of the blast. The model approximated the underwater portion of the crater based on variations in water color that likely correspond to the crater depth. The contour was approximated as an ellipse using a linear conic fitting method. We note that the estimated crater depth along the major axis is similar to an estimate provided in Sadek et al. (2022) based on an in-person survey. Figure S4 shows the satellite image zoomed in on the blast crater region with the outline of the estimated ellipse overlaid.



Figure S4: Post-Sentinel-2 colored satellite image taken on August 8, 2020 with the approximated crater geometry overlaid in green. The crater geometry was approximated using the Segment Anything Model.

S2.3 SAR Architecture

We apply SpikeAD with 4 iterations over 11×11 pixel neighborhoods, providing aggressive despeckling while maintaining damage region boundaries. Figure S5 demonstrates that this procedure effectively reduces speckle noise which is visible as isolated bright pixels in the original acquisition, while preserving contiguous damage signatures, with modifications concentrated in isolated locations rather than structured damage regions.

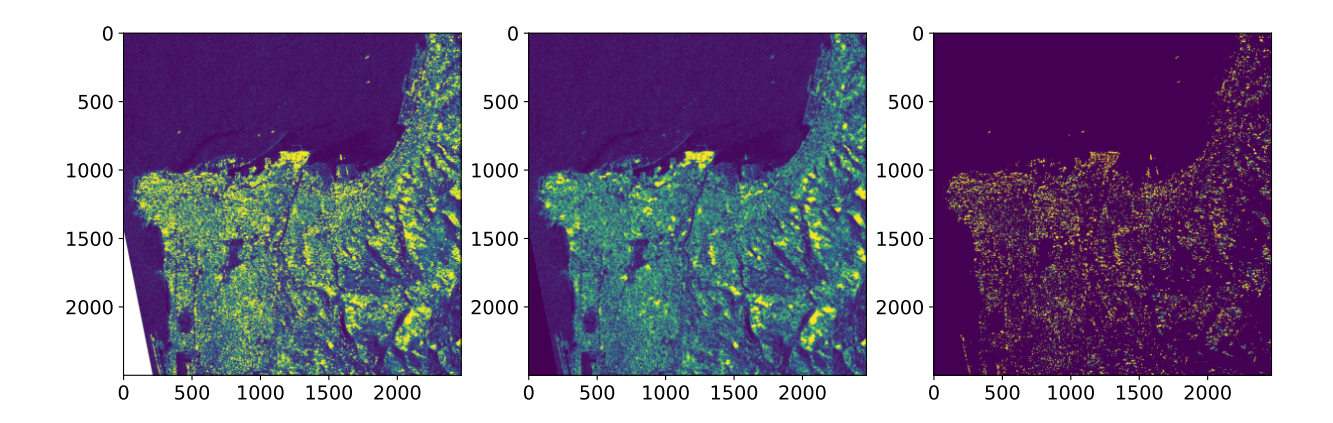


Figure S5: Sentinel-1 SAR imagery from August 5, 2020: (left) original acquisition, (middle) despeckled via SpikeAD, (right) difference highlighting modified pixels. The algorithm predominantly affects isolated speckle rather than structured damage regions, validating the approach.

Figure S5 shows how SpikeAD can be used spatially to remove speckle and noise, especially in the water, while enhancing the contrast of some features, such as the port area in the center. SpikeAD is a smoothing technique (employing "intelligent" median-filtering), but this means that some signal might get smoothed out. This selective modification proves particularly effective for SAR speckle, where noise manifests as isolated high-intensity pixels rather than spatially coherent patterns.

One goal for using SpikeAD here was to maintain as much original signal from the SAR images while removing the speckle noise. We also wanted to characterize what had changed from before to after the event (the Beirut blast in this instance). One way to use SpikeAD here is across time. In this research, SpikeAD is used temporally instead of spatially, as it is typically employed (Figure S5). For use of SpikeAD across time, we employ 1x1 neighborhoods (i.e., each pixel is handled independently across time). Figure S6 shows how SpikeAD is used to generate a composite image (bottom) for July, 2020 for ascending relative orbit 14 (A14) images (top).

Figure S7 shows SpikeAD applied to A14 SAR images for August, 2020. Now the coherence image for A14 is computed using these two composite images (bottom image in Figure S6 and bottom image in Figure S7), which can be seen int Figure S8. The process is repeated for ascending relative orbit 87 (A87; figures not shown) as well as descending relative orbit 21 (D21; Figures S9, S10 and S11) and descending relative orbit 94 (D94, figures not shown). Finally, the combined damage map is computed from the 4 coherence images by aggregating them together (pixel-wise addition followed by normalization between 0 and 1) and then computing the damage percentage across 10x10 windows, see Figure S12.

Once the coherence maps are constructed and converted into D%, they are subjected to a check to ensure that they resemble damage maps caused by a radially weakening blast wave. The D% map is divided into 15 annular zones centered at the blast epicenter, thus binning the damage aggregation boxes as a function of their epicentral distance. In Figure S14 in Appendix S1.3 (left), in each bin/annular zone, we plot the $95^{\rm th}$ percentile of the damage percent (D%) as a function of the epicentral distance; it confirms physically consistent radial decay of damage percentage. This trend holds true for lower percentiles too (up to $80^{\rm th}$), indicating that the effect of noise at these higher percentiles is muted. In Figure S14 (right), we plot the number of pixels of the coherence maps that are in each annual zone above the $80^{\rm th}$, $90^{\rm th}$ and $95^{\rm th}$ percentile thresholds and we see an approximately uniform spatial sampling across zones, preventing any single distance range from dominating the inference. The retained boxes typically exhibit damage percentages ranging from 40–100%, concentrated within 2 km of the epicenter with gradual decrease to 10–30% at 5 km distance.

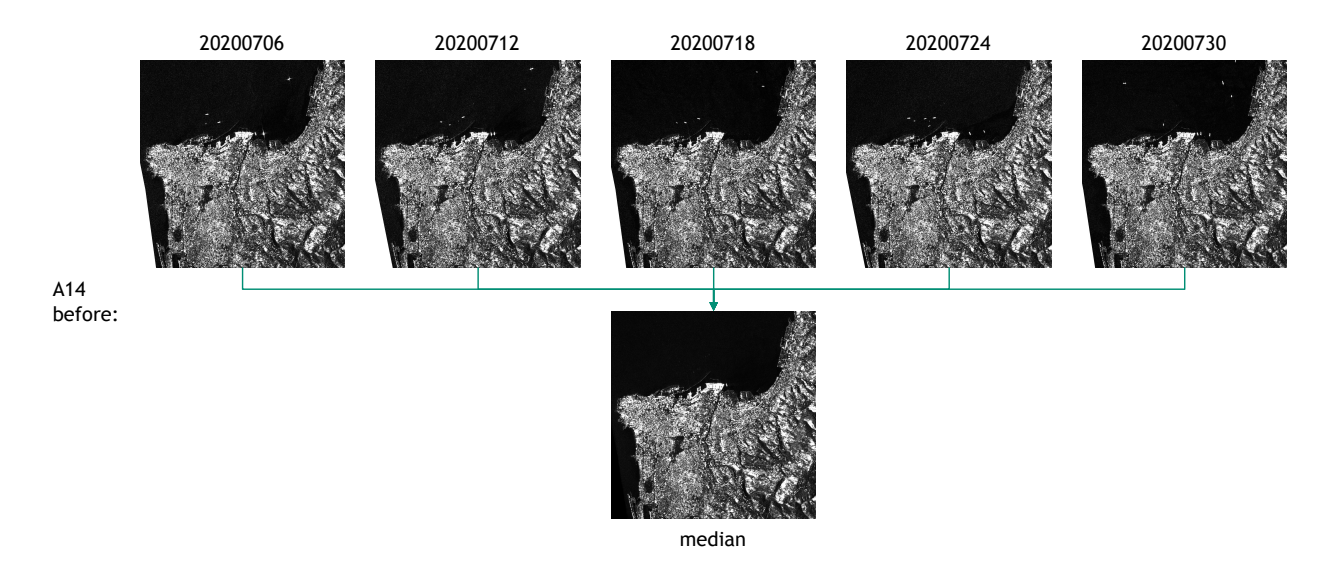


Figure S6: Sentinel-1 SAR imagery from ascending relative orbit 14 for July, 2020: (top) original acquisition, (bottom) despeckled via SpikeAD. The algorithm predominantly affects isolated speckle rather than structured damage regions (such as those in the water), validating the approach.

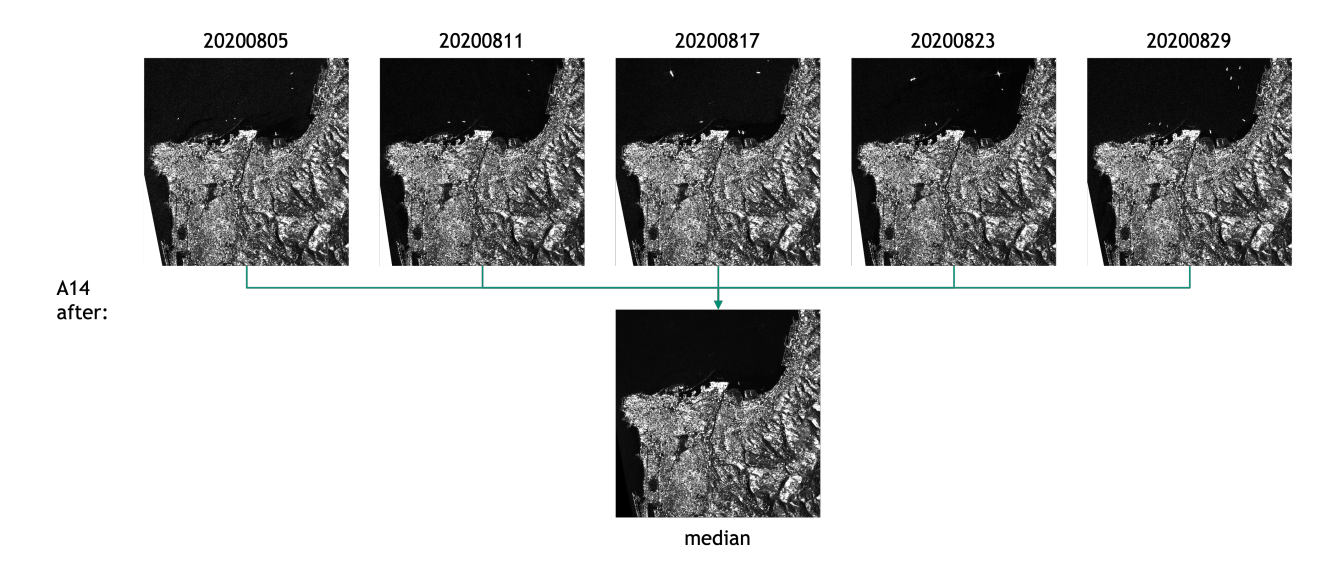


Figure S7: Sentinel-1 SAR imagery from ascending relative orbit 14 for August, 2020: (top) original acquisition, (bottom) despeckled via SpikeAD. \cdot

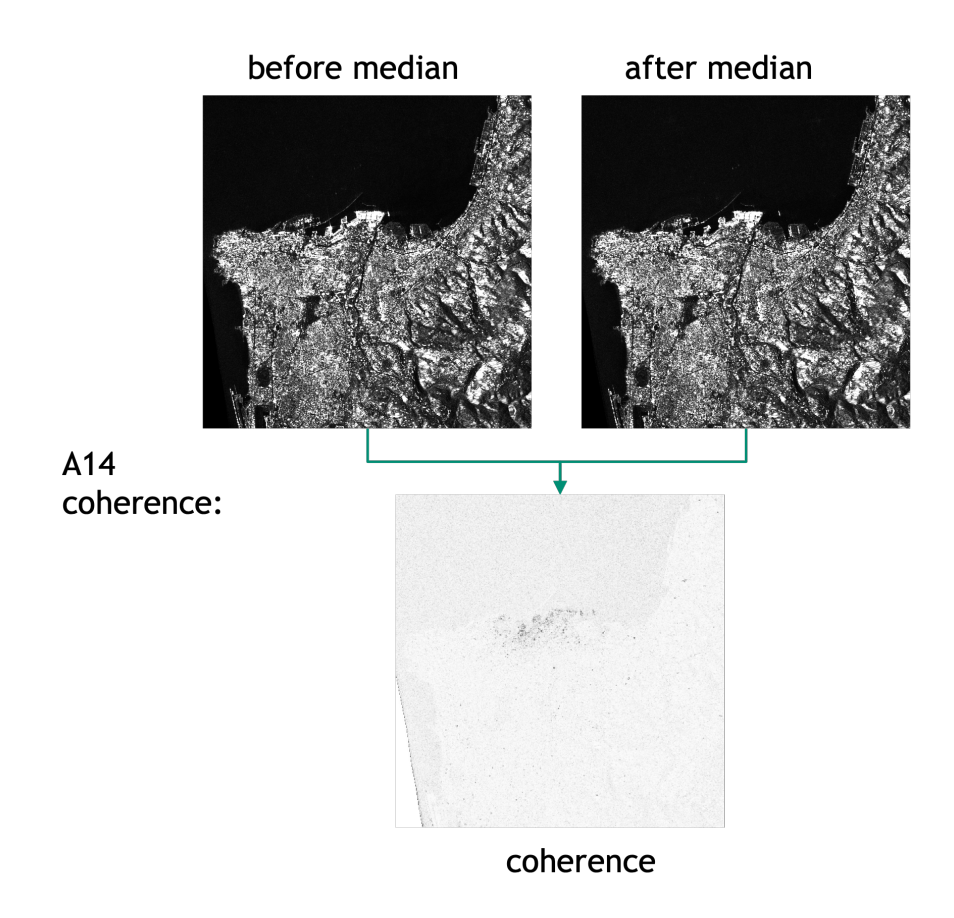


Figure S8: Coherence image (bottom) for ascending relative orbit 14 between July (top-left) and August (top-right), 2020.

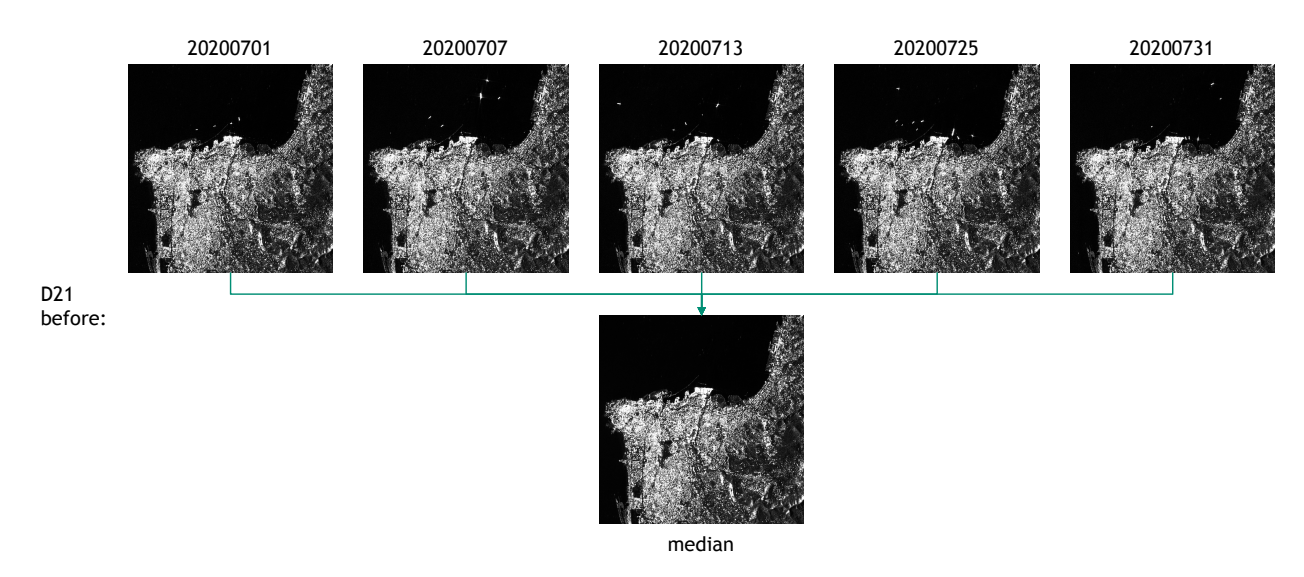


Figure S9: Sentinel-1 SAR imagery from descending relative orbit 21 for July, 2020: (top) original acquisition, (bottom) despeckled via SpikeAD.

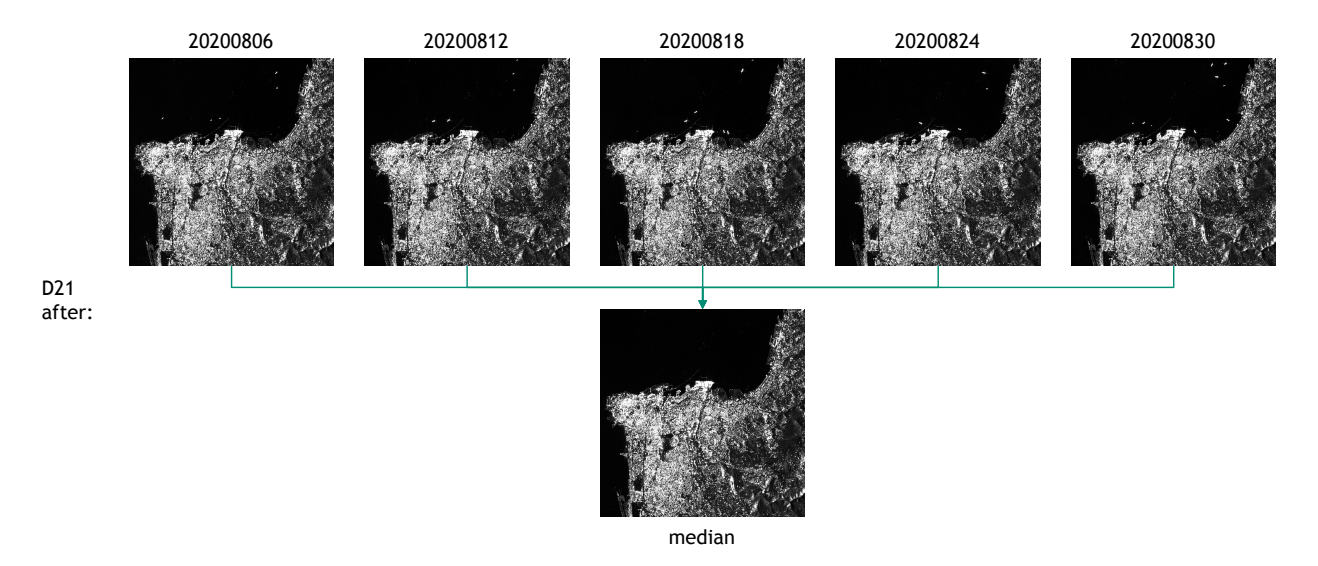


Figure S10: Sentinel-1 SAR imagery from descending relative orbit 21 for August, 2020: (top) original acquisition, (bottom) despeckled via SpikeAD. \cdot

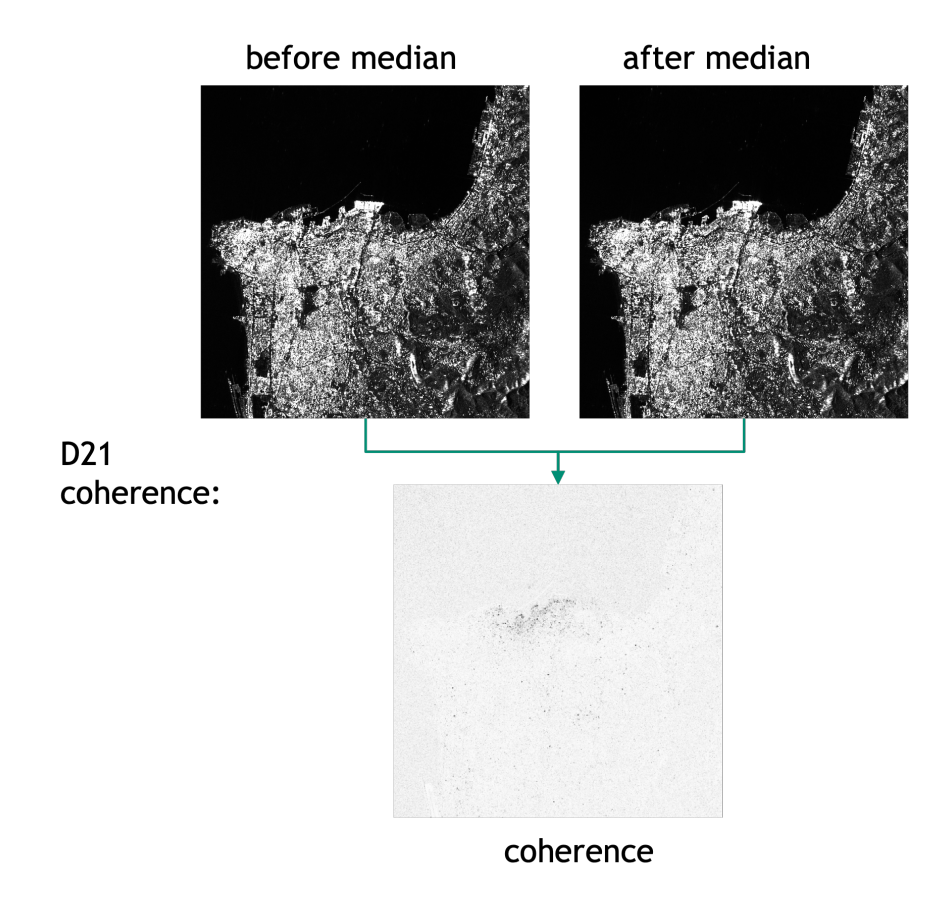


Figure S11: Coherence image (bottom) for descending relative orbit 21 between July (top-left) and August (top-right), 2020.

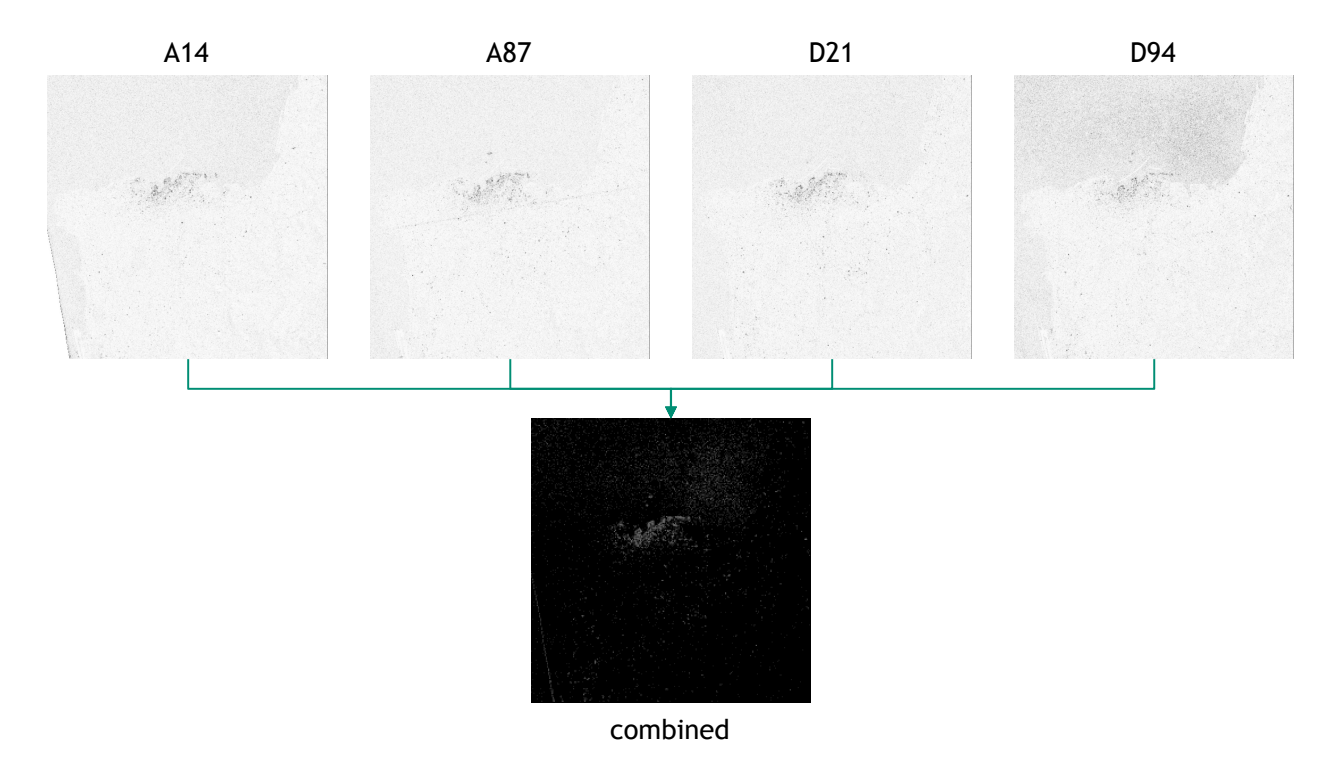


Figure S12: Combined damage map.

The despeckling process described above provided damage estimates that were too smooth in space, i.e., the decay in damage levels with distance from the epicenter was too shallow. Fitting an over-pressure model led to a yield estimate of about 5 kt which was too large to be credible. Consequently, we did not pursue the process any further for post-processing the SAR images.

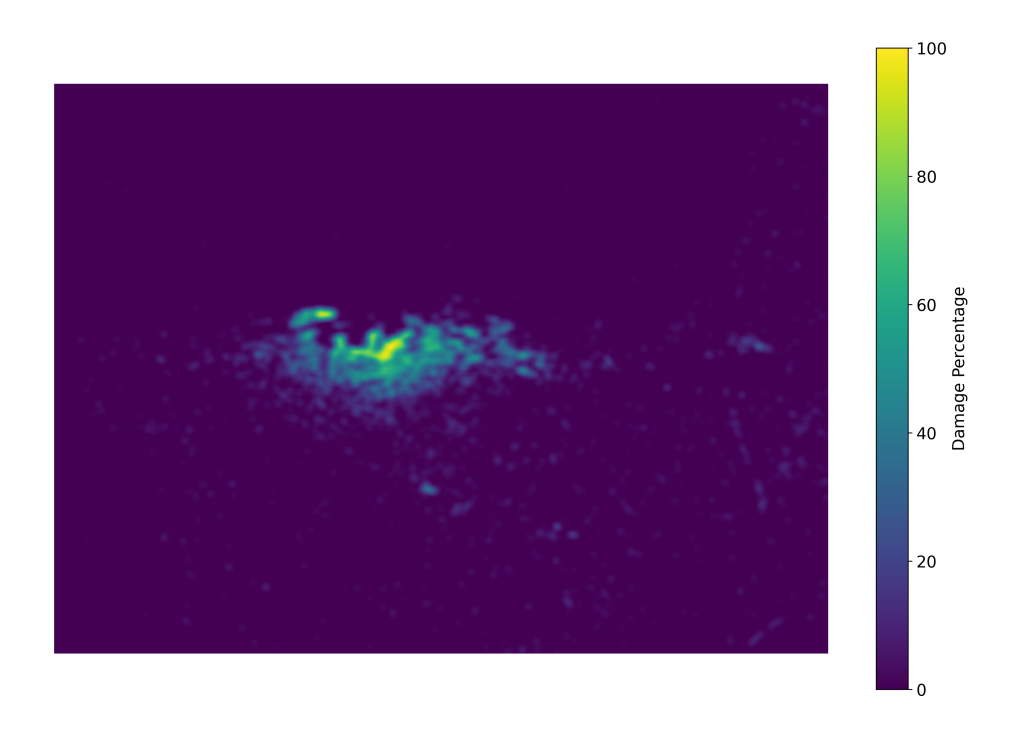


Figure S13: Composite damage map computed using the data from Pilger and colleagues (Pilger et al., 2021).

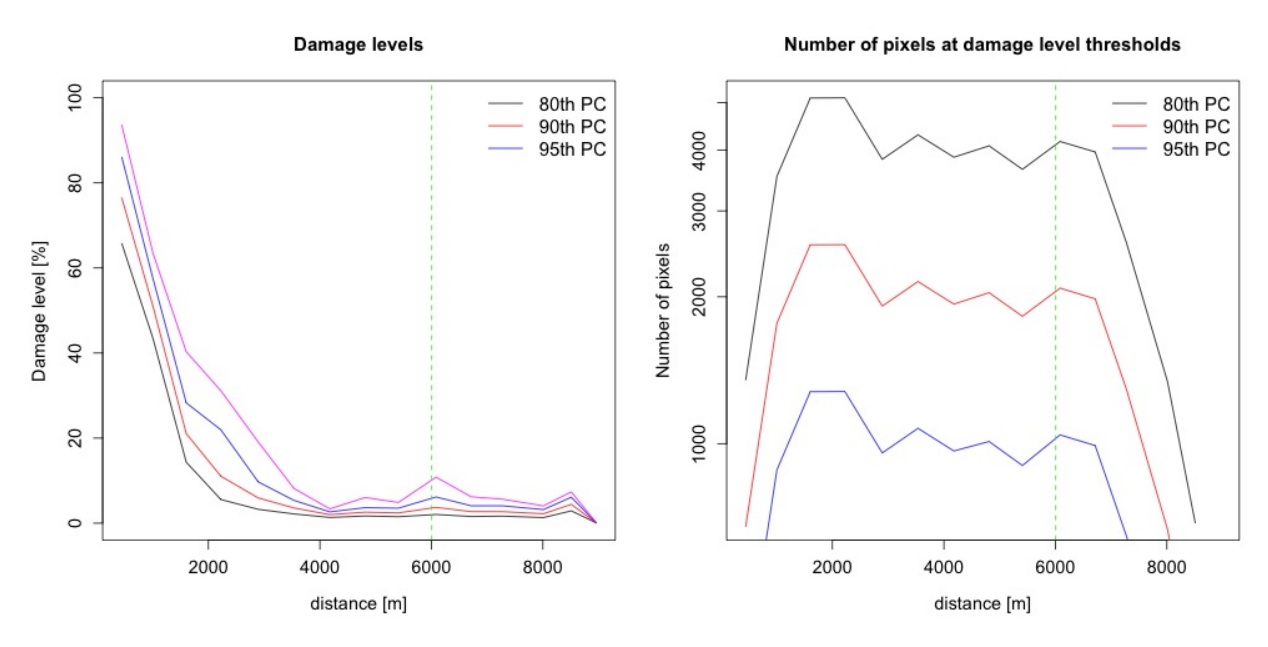


Figure S14: Spatial distribution after zonal thresholding. (Left) Radial decay of average damage at 80th, 90th, 95th percentile thresholds demonstrates physically consistent overpressure relaxation. Horizontal axis shows median distance of retained boxes in each zone. (Right) Number of retained boxes per zone confirms approximately uniform spatial sampling. PC denotes percentile.

S2.4 Vision-Language Model Architecture for Damage Assessment

Model Selection and Variants

We employed the Google Gemma-3 family of vision-language models for automated blast damage assessment from street-level imagery. Gemma-3 represents Google's latest open-weight multimodal models, incorporating the SigLIP vision encoder for joint processing of text and images. We systematically evaluated three parametric variants to assess the relationship between model capacity and damage assessment quality:

- google/gemma-3-4b-it: 4 billion parameters (baseline)
- google/gemma-3-12b-it: 12 billion parameters (intermediate)
- google/gemma-3-27b-it: 27 billion parameters (maximum capacity)

Each model employs a decoder-only transformer architecture with grouped-query attention and processes visual inputs through square images resized to 896×896 pixels. The instruction-tuned variants (-it) were selected for their superior performance on structured output tasks. All models support a 128K token context window (except the 1B variant with 32K), enabling processing of extensive contextual information alongside visual inputs. For this analysis we constrained the output to the use of the 27B variant, given that while all models demonstrated reasonable potential to map damage categories to overpressure estimates, the 27B variant consistently produced an overpressure-distance relationship that better conformed to expected blast physics, exhibiting smoother spatial decay, reduced local variability, and improved adherence to theoretical power-law attenuation with distance from the epicenter.

MMLU-Style Probabilistic Assessment Framework

Rather than generating deterministic classifications, we adapted the MMLU (Massive Multitask Language Understanding) evaluation methodology commonly used in language model benchmarking to produce probability mass functions (PMFs) over damage categories. This approach transforms visual damage assessment into a constrained single-token generation task, enabling rigorous uncertainty quantification.

The damage categorization framework consists of nine discrete categories (levels 0-8), each corresponding to specific overpressure ranges and observable structural effects:

Level	Category	Pressure Range (psi)
0	No blast damage	0
1	Glass/Noise Effects	0.04-0.15
2	Limited Structural Effects	0.15-0.40
3	Window/Housing Damage	0.40-1.0
4	Home Inhabitability Issues	1.0-2.0
5	Significant Structural Collapse	2.0-3.0
6	Major Structural Failures	3.0-5.0
7	Near-Complete Destruction	5.0-7.0
8	Catastrophic Destruction	>7.0

Table S8: Blast Damage Assessment Rubric for VLM Classification

For each image i and damage level $k \in \{0, 1, \dots, 8\}$, we calculate the conditional log-likelihood of the model generating token "k" as the continuation:

$$\ell_{ik} = \log \mathbb{P}(\text{token} = \text{``k''} \mid \text{image}_i, \text{prompt})$$
 (S2)

The raw log-likelihoods undergo numerical stabilization through the log-sum-exp transformation to yield properly normalized probabilities:

$$q_{ik} = \frac{\exp(\ell_{ik} - \max_{j} \ell_{ij})}{\sum_{m=0}^{8} \exp(\ell_{im} - \max_{j} \ell_{ij})}$$
(S3)

This produces a PMF $\mathbf{q}_i = \{q_{i0}, q_{i1}, \dots, q_{i8}\}$ for each image, ensuring numerical stability while maintaining relative probability relationships between damage levels.

Prompt Engineering

The prompt structure incorporates several key design elements to optimize damage assessment performance. Each prompt begins with a task specification establishing the model's role as a damage assessment system, followed by the image token placeholder which is replaced by the model's visual encoding. Metadata fields including capture date and GPS coordinates from the Mapillary dataset provide spatial and temporal context.

The damage level categories are explicitly enumerated with their corresponding pressure ranges, ensuring the model has complete information about the classification schema. Assessment criteria direct attention to structural elements most indicative of blast damage, including window breakage, wall collapse, roof damage, debris patterns, and overall structural integrity. The prompt concludes with the instruction "Answer: " followed by a space character, constraining the model to generate a single digit (0-8) as the next token.

This formulation enables calculation of log-likelihoods for each possible damage level in a single forward pass, providing computational efficiency for processing hundreds of images.

Uncertainty Quantification

Classification uncertainty is quantified through Shannon entropy calculated over each PMF using natural logarithm:

$$H(\mathbf{q}_i) = -\sum_{k=0}^{8} q_{ik} \ln(q_{ik})$$
 (S4)

Conversion to Expected Overpressure

Each PMF is converted to an expected overpressure value using a weighted average:

$$\hat{\psi}_i = \sum_{k=0}^8 q_{ik} \cdot \psi_k \tag{S5}$$

where ψ_k represents the characteristic pressure for damage level k, defined in the damage-to-PSI mapping: $\{0:0.0,1:0.095,2:0.28,3:0.705,4:1.55,5:2.55,6:4.05,7:6.05,8:8.0\}$ psi. These characteristic values represent the midpoint or representative pressure for each damage category, derived from blast engineering literature.

This expected overpressure $\hat{\psi}_i$, combined with the GPS coordinates of each image, provides the observational data for subsequent blast yield estimation through integration with Kingery-Bulmash models, with the entropy-derived weights w_i enabling robust regression that downweights uncertain classifications.

Processing Pipeline

The complete analysis pipeline processes geolocated Mapillary images through the following workflow: (1) images are loaded with GPS metadata and resized to 896×896 pixels; (2) prompts are constructed with metadata fields populated for each image; (3) log-likelihoods are computed for all nine damage levels in a single forward pass; (4) PMFs are extracted via the log-sum-exp transformation; (5) uncertainty metrics including Shannon entropy and confidence scores are calculated; and (6) expected overpressures are computed for integration with blast physics models.

S3 Results

Hyperparameter Posteriors by Modality

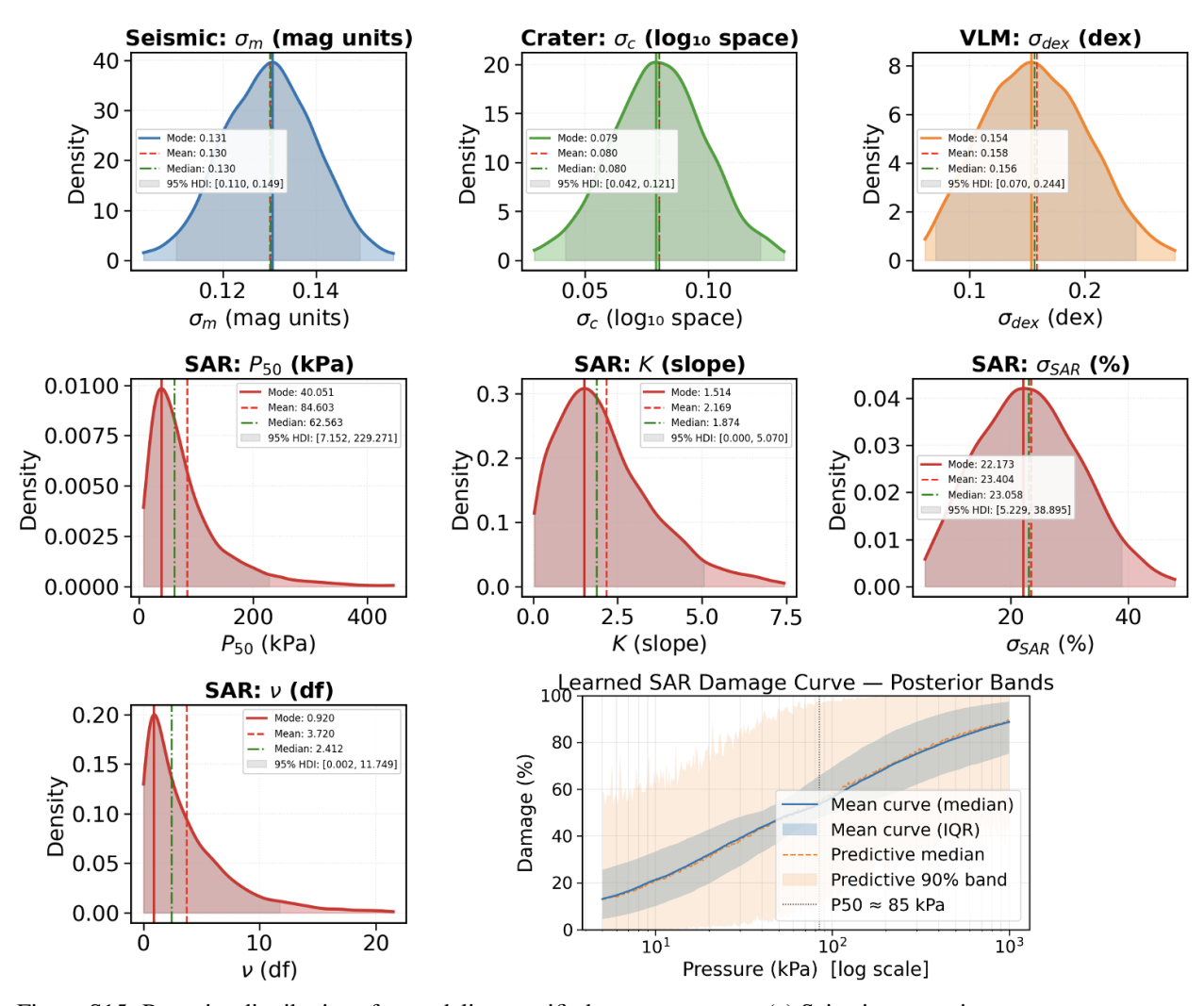


Figure S15: Posterior distributions for modality-specific hyperparameters. (a) Seismic uncertainty σ_m converges near 0.13 magnitude units. (b) Crater uncertainty $\sigma_c \approx 0.08$ in log-space, corresponding to $\sim\!20\%$ linear uncertainty. (c) VLM uncertainty $\sigma_{\rm dex}$ reflects damage classification spread. (d-g) SAR parameters: P_{50} indicates 50% damage threshold, K controls transition steepness, $\sigma_{\rm SAR}$ quantifies scene heterogeneity, and ν indicates moderate tail heaviness. Vertical dashed lines indicate prior means; solid distributions show learned posteriors. h) Learned damage to overpressure relationship using SAR imagery.

S3.1 Validation Through Posterior Predictive Checks

To validate that the multimodal fusion framework produces a well-calibrated model consistent with observations, we perform posterior predictive checks (Gelman et al., 1996; Gabry et al., 2019). These checks assess whether data generated from the posterior distribution resembles the observed data, providing crucial validation that our model captures the essential physics while appropriately quantifying uncertainties.

For each modality i, we generate replicated datasets $\tilde{\mathbf{D}}_i^{\text{rep}}$ by:

- 1. Drawing samples $(Y^{(s)}, \theta_i^{(s)})$ from the joint posterior $p(Y, \theta_i | \mathbf{D})$.
- 2. Generating synthetic observations using the forward model: $\tilde{\mathbf{D}}_i^{\text{rep}} \sim \mathcal{F}(\mathbf{D}_i | Y^{(s)}, \boldsymbol{\theta}_i^{(s)})$.

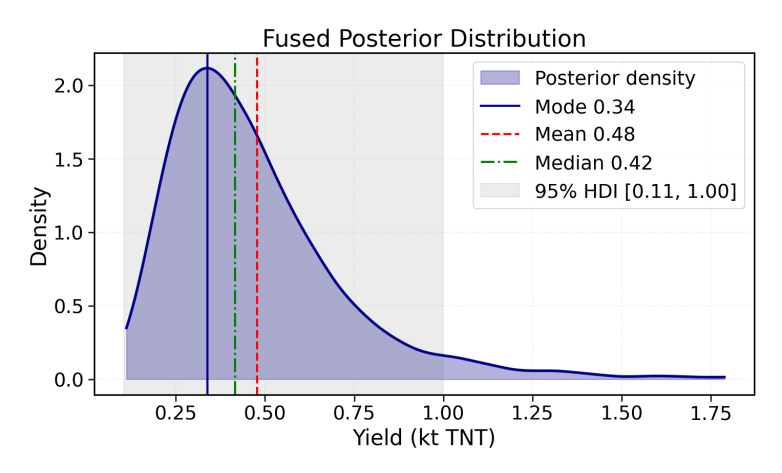


Figure S16: Fused posterior distribution for explosive yield combining all four modalities.

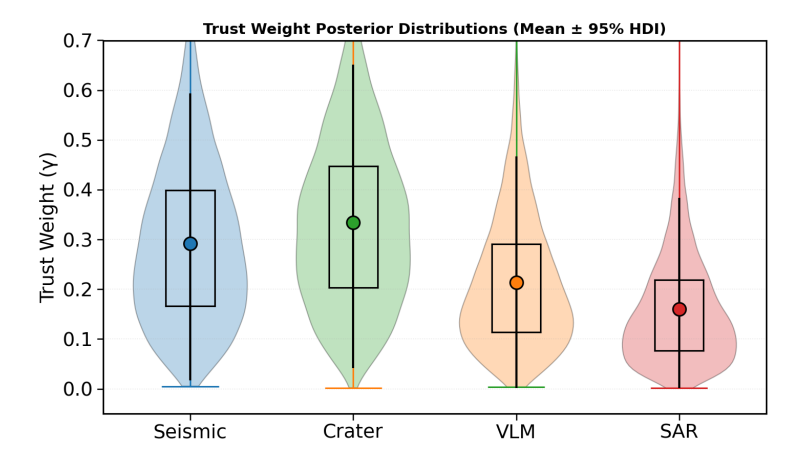


Figure S17: Learned trust weights for each modality. Box plots show posterior means (dots), interquartile ranges (boxes), and 95% HDIs (whiskers). Distributions are overlapping due to the simplex constraint $\sum \gamma_i = 1$.

3. Computing test statistics $T(\tilde{\mathbf{D}}_i^{\text{rep}})$ and comparing to observed $T(\mathbf{D}_i)$.

The posterior predictive p-value for test statistic T is defined as:

$$p_{\text{Bayes}} = \mathbb{P}(T(\tilde{\mathbf{D}}^{\text{rep}}) \ge T(\mathbf{D})|\mathbf{D}) = \int \mathbb{I}[T(\tilde{\mathbf{D}}^{\text{rep}}) \ge T(\mathbf{D})] \, p(\tilde{\mathbf{D}}^{\text{rep}}|\mathbf{D}) \, d\tilde{\mathbf{D}}^{\text{rep}}, \tag{S6}$$

where $\mathbb{I}[\cdot]$ is the indicator function. Values of $p_{\text{Bayes}} \approx 0.5$ indicate good calibration, while extreme values near 0 or 1 suggest model misspecification. This is computed using S=1000 posterior-predictive Monte Carlo replicates per modality with the discrepancy functions provided in Table S9.

For our posterior predictive checks, we use Monte Carlo integration to compute (S6). Specifically, we approximate p_{Bayes} using posterior draws and posterior-predictive replicates. Letting $\{(Y^{(s)}, \boldsymbol{\theta}_i^{(s)})\}_{s=1}^S \sim p(Y, \boldsymbol{\theta}_i \mid \mathbf{D})$ be S MCMC sample, for each draw, we simulate a replicate dataset $\tilde{\mathbf{D}}_i^{(s)} \sim p(\tilde{\mathbf{D}}_i \mid Y^{(s)}, \boldsymbol{\theta}_i^{(s)})$ via the same forward models \mathbf{F}_i used for fitting, then evaluate the discrepancy $T(\tilde{\mathbf{D}}_i^{(s)})$. With $T_{\text{obs}} = T(\mathbf{D}_i)$ we estimate

$$\widehat{p}_{\mathrm{Bayes}} = \frac{1}{S} \sum_{s=1}^{S} \mathbb{I} \left\{ T(\widetilde{\mathbf{D}}_{i}^{(s)}) \geq T_{\mathrm{obs}} \right\}, \qquad \mathrm{SE}(\widehat{p}_{\mathrm{Bayes}}) \approx \sqrt{\frac{\widehat{p}_{\mathrm{Bayes}} \left(1 - \widehat{p}_{\mathrm{Bayes}}\right)}{S}}.$$

For discrete T (ties), we report the mid-p:

$$\widehat{p}_{\text{Bayes}}^{\text{mid}} = \frac{1}{S} \sum_{s=1}^{S} \mathbb{I} \big\{ T(\tilde{\mathbf{D}}_{i}^{(s)}) > T_{\text{obs}} \big\} \ + \ \frac{1}{2S} \sum_{s=1}^{S} \mathbb{I} \big\{ T(\tilde{\mathbf{D}}_{i}^{(s)}) = T_{\text{obs}} \big\}.$$

Unless otherwise stated, we use S=1000 replicates (per modality) and report \hat{p}_{Bayes} with its Monte Carlo standard error.

Table S9: Posterior-predictive discrepancies $T(\cdot)$ used.

Modality	Observed	Discrepancy $T(\cdot)$
Seismic (M_w)	M_w	$T_m = \frac{\left(M_w - M_w^{\text{pred}}(Y)\right)^2}{\sigma_m^2}$
$\operatorname{Crater}\left(z = \log_{10} D\right)$	$z_{ m obs}$	$T_c = rac{ig(z_{ m obs} - \mu_c(Y)ig)^2}{\sigma_c^2}$
SAR (damage logits)	$\{z_i\}_{i=1}^{N_{SAR}}$	$T_{\text{SAR}} = \frac{1}{N_{\text{SAR}}} \sum_{i=1}^{N_{\text{SAR}}} \left[-\log f_{t_{\nu}} \left(z_i \mid z_{\mu,i}(Y), \frac{\sigma_{\text{SAR}}}{100} \right) \right]$
VLM (9-bin PMFs)	$\{q_{ik}\}$	$T_{\text{VLM}} = \frac{1}{N_{\text{VLM}}} \sum_{i=1}^{N_{\text{VLM}}} \sum_{k=0}^{8} \left[- q_{ik} \log \pi_{ik}(P_i(Y), \sigma_{\text{dex}}) \right]$

Figure S18 presents the posterior predictive distributions for all four modalities. The seismic modality (panel a) yields $p_{\rm Bayes}=0.78$, indicating the observed magnitude falls slightly below the predictive median, though which is consistent with poor seismic coupling in the near-shore environment. The crater modality (panel b) achieves near-perfect calibration with $p_{\rm Bayes}=0.51$, validating the crater scaling relationship and uncertainty quantification. Both modalities' individual posterior predictive distributions also cover the observed values. For the damage modalities, the VLM predictions (panel c) successfully capture the observed PMF structure across the damage categories, with observed probabilities falling within the interquartile ranges of predicted distributions. The SAR predictions (panel d) demonstrate that the learned vulnerability curve with $P_{50}=83.6$ kPa and slope K=2.14 reproduces the spatial decay of damage, with most observations falling within the 90% credible interval. These checks confirm that the fractional posterior framework neither overfits to individual modalities nor produces overconfident predictions, with the good agreement across fundamentally different observables providing good evidence for validating both the physics-based forward models and the learned hyperparameters.

S3.2 Leave-One-Out Validation and Trust Weight Verification

To verify the learned trust weights, we perform leave-one-out (LOO) validation by systematically removing each modality and measuring the resulting change to the fused posterior. The information loss is quantified by Kullback-Leibler divergence:

$$D_{\mathrm{KL}}(p_{\mathrm{full}} \| p_{-k}) = \int p(Y | \mathcal{D}_{\mathrm{all}}) \log \frac{p(Y | \mathcal{D}_{\mathrm{all}})}{p(Y | \mathcal{D}_{-k})} \, \mathrm{d}Y, \tag{S7}$$

where larger KL divergence indicates greater posterior shift when modality k is excluded.

Figure S19 reveals the nuanced relationship between modality agreement and posterior influence. Removing SAR produces the largest KL divergence (0.165), confirming its role as the most discordant modality despite receiving the lowest trust weight ($\gamma_{SAR}=0.15$). The substantial posterior shift upon SAR's removal demonstrates that even down-weighted modalities contribute meaningfully to the fused distribution, particularly by expanding uncertainty bounds to reflect model disagreement.

VLM exhibits intermediate behavior with KL divergence of 0.120, consistent with its moderate trust weight ($\gamma_{\text{VLM}} = 0.22$). The damage-based modalities thus both pull the posterior toward higher yields while contributing substantial uncertainty, appropriately captured by their lower trust weights.

Remarkably, seismic and crater exhibit nearly identical KL divergences (0.098 and 0.096 respectively), despite their different trust weights ($\gamma_{\text{seismic}} = 0.28$ and $\gamma_{\text{crater}} = 0.34$). This near-equivalence reflects their convergent modal estimates (both 0.34 kt) and their role as the primary anchors of the fused posterior. The minimal posterior shift when either is removed indicates that the remaining modality can largely compensate, confirming their mutual consistency and the robustness of the yield estimate.

The single-modality posteriors (dotted lines) further illuminate this structure: seismic produces a sharp, high-confidence posterior centered at 0.34 kt, while crater shows similar central tendency with slightly broader uncertainty. The damage-based modalities (VLM and SAR) exhibit substantially wider distributions with heavier tails extending to higher yields,

Posterior Predictive Checks — with Individual PDFs

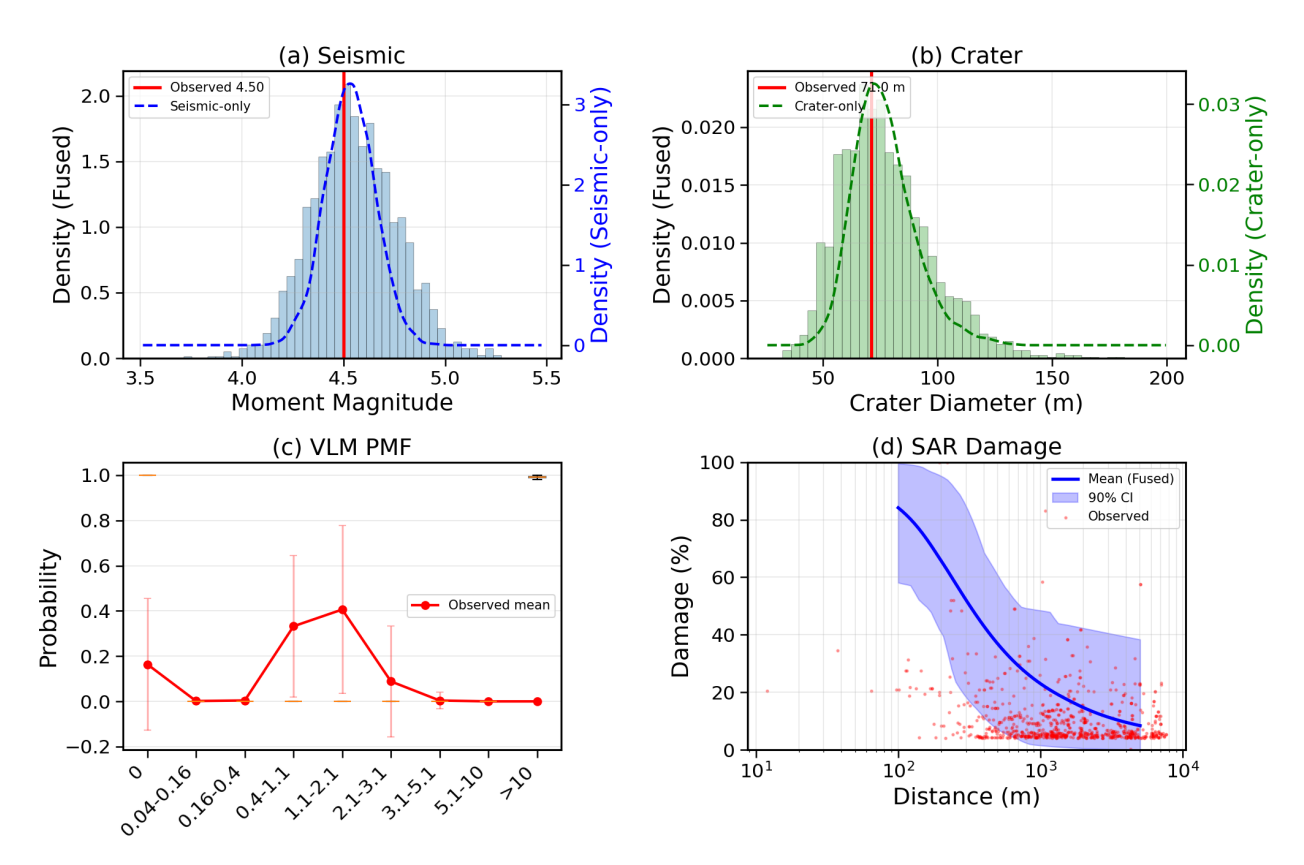


Figure S18: Posterior predictive histograms for all modalities against individual posteriors (dotted) (a) Seismic: predicted moment magnitude distribution (blue) versus observed $M_w=4.50$ (red line), p=0.78. (b) Crater: predicted diameter distribution (green) versus observed 71 m (red line), p=0.51. (c) VLM: predicted PMF distributions (boxplots) versus observed mean PMF (red line with error bars). (d) SAR: predicted damage versus distance with 90% CI (blue band) and observations (red dots). P-values near 0.5 indicate well-calibrated predictions without systematic bias.

justifying their lower trust weights. The fractional fusion framework successfully identifies and appropriately weights these heterogeneous information sources, with the learned trust weights reflecting both precision and agreement with the emerging consensus.

S3.3 Additional fusion studies: design, scenarios, and results

Objective and setup. We stress—test the fusion under controlled misspecification using a four—modality generator with a single latent yield Y^* (kt). The generator mirrors the forward models used in the main analysis: KB overpressure for blast physics, a SAR vulnerability curve on the logit scale, and a 9-bin VLM pressure—binning model. Seismic and crater use the affine links in Sec. 4. The latent truth is fixed to $Y^* = 0.30 \, \mathrm{kt}$ (alternative values give qualitatively similar conclusions).

Scenarios (inputs). We consider five minimal stress scenarios chosen to mimic the qualitative behavior of the Beirut data. Table S10 lists the settings (sample sizes, tail–heaviness ν , pressure bias δ in \log_{10} –kPa, VLM mislabel rate η , and a shared dependence shock ρ). Here δ =0.35 corresponds to a \sim 2.2× pressure bias.

Data generation. For seismic, $M_w = a \log_{10} Y^* + b + \varepsilon_m$, $\varepsilon_m \sim \mathcal{N}(0, \sigma_m^2)$ with (a, b) = (3.0, -1.2) and $\sigma_m \in \{0.10, 0.16\}$. For crater, $z = \log_{10} D = c \log_{10} Y^* + d + \varepsilon_c$, $\varepsilon_c \sim \mathcal{N}(0, \sigma_c^2)$ with (c, d) = (1.0, 1.2) and $\sigma_c \in \{0.05, 0.09\}$. For SAR, ranges $r \sim \text{LogUniform}(r_{\min}, r_{\max})$; $P_{\psi}(r, Y^*) \rightarrow \log_{10} P_{k\text{Pa}}$ enters the vulnerability

Leave-One-Out Validation

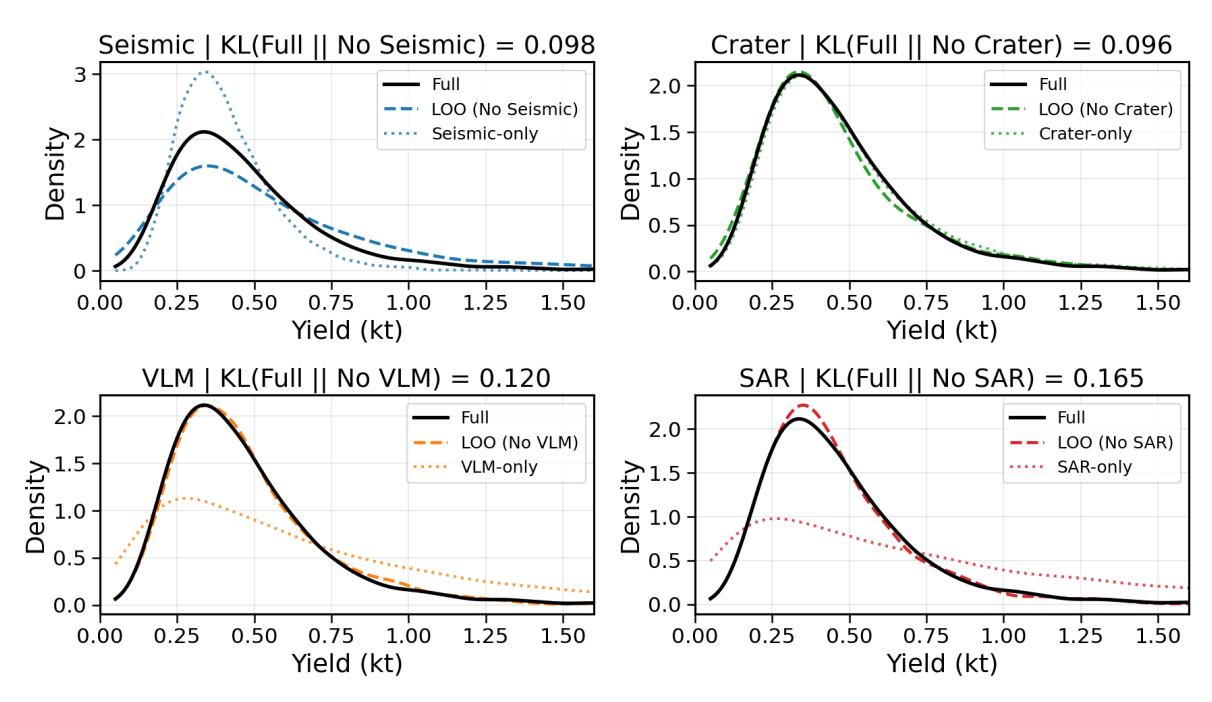


Figure S19: Leave-one-out validation comparing the full fused posterior (solid black) with posteriors after removing individual modalities (dashed lines) and single-modality posteriors (dotted lines). KL divergence values quantify the posterior shift when each modality is removed.

Table S10: Synthetic stress scenarios used in Sec. S3.3.

Scenario	N_{SAR}	ν	δ	$\sigma_{ m SAR}$	$N_{ m VLM}$ / η	ρ	
Base clean	120	8	0.00	40	160 / 0.00	0.0	
SAR heavy-tail	120	2.5	0.00	40	160 / 0.00	0.0	
SAR biased	120	8	0.35	40	160 / 0.00	0.0	
VLM noisy	120	8	0.00	40	160 / 0.10	0.0	
Dependence $\rho = .6$	120	8	0.00	40	160 / 0.00	0.6	

curve $\mu(r)=100 \left(1+\exp\{-K[\log_{10}P_{\mathrm{kPa}}(r)-\log_{10}P_{50}]\}\right)^{-1}$; logits $z_{\mu}(r)=\log\mathrm{it}(\mu/100)$ generate $z_{\mathrm{obs}}(r)\sim t_{\nu}(z_{\mu}(r),\sigma_{\mathrm{SAR}}/100)$; optional bias applies $\log_{10}P_{\mathrm{kPa}}\leftarrow\log_{10}P_{\mathrm{kPa}}+\delta$. For VLM, $P_{\psi}(r,Y^{\star})\rightarrow\Pi(r)$ via logistic binning with spread s_{dex} ; mislabel noise is $Q(r)=(1-\eta)\Pi(r)+\eta/9$. Dependence is injected by a shared Gaussian shock Z with correlation ρ into seismic, crater, and SAR residuals; VLM noise remains independent.

S3.3.1 Fusion models (ablations) and metrics

Let $\mathcal{L}_i(Y)$ be each modality's log–likelihood. We compare:

(i) Plain product:
$$\log \pi(Y \mid \mathrm{data}) \propto \sum_i \mathcal{L}_i(Y),$$

(ii) Single temperature:
$$\beta \sum_{i} \mathcal{L}_{i}(Y), \quad \beta \sim \text{Beta}(4,2)$$

(iii) Fixed- γ (CV): $\sum_i \gamma_i \mathcal{L}_i(Y)$ (γ from the single–modality expected log predictive density softmax)

(iv) Dirichlet-
$$\gamma$$
: $\sum_{i} \gamma_{i} \mathcal{L}_{i}(Y)$, $\gamma \sim \text{Dirichlet}(\mathbf{1}_{4})$.

For each scenario and method we report: (a) coverage of the 95% HDI for Y^* (mean over replicates), (b) sharpness (median HDI width), (c) accuracy (RMSE of the posterior median). For the proposed model we also summarize the mechanism via median posterior—mean $\bar{\gamma}$ of the intentionally corrupted modality.

S3.3.2 Experimental results

Experiment A: Base clean. All modalities are well–specified. In Fig. S20, the tempered methods (Single– α , Fixed– γ , Dirichlet– γ) achieve near–nominal coverage with similar widths, while the plain product is optimistic (coverage ≈ 0 due to overconfidence). In Fig. S21 (Base clean bars), RMSE is comparable across tempered methods and smallest for Dirichlet– γ .

Experiment B: SAR heavy-tail ($\nu=2.5$). Only SAR is misspecified (heavier tails). In Fig. S20, the plain product under–covers; Dirichlet– γ preserves $\approx 95\%$ coverage with competitive width. Fig. S21 shows reduced RMSE under Dirichlet– γ relative to baselines. The mechanism summary (Table S11) reports a low median trust weight for corrupted SAR.

Experiment C: SAR biased ($\delta = 0.35$). A systematic upward shift in \log_{10} -kPa. Coverage-width points in Fig. S20 again place Dirichlet- γ on the favorable frontier; RMSE in Fig. S21 is lowest among the comparators. Table S11 shows further down-weighting of SAR.

Experiment D: VLM noisy ($\eta=0.10$). Only VLM labels are corrupted. Dirichlet– γ maintains near–nominal coverage with narrow intervals (Fig. S20) and competitive RMSE (Fig. S21); the median $\bar{\gamma}$ shifts away from VLM (Table S11).

Experiment E: Cross-modality dependence ($\rho = 0.6$). Moderate redundancy is introduced via a shared shock. Table S13 summarizes a mild coverage degradation across all methods; Dirichlet- γ remains closest to nominal with competitive width.

Experiment F: BMA (Bayesian Model Averaging). BMA treats each modality as a separate model and weights posterior samples by model evidence. For each modality i, we fit a single-modality model, compute WAIC (Widely Applicable Information Criterion) as an approximation to out-of-sample predictive accuracy, and define weights $w_i \propto \exp(\text{ELPD}_i)$ where $\text{ELPD}_i = -\frac{1}{2}\text{WAIC}_i$ converts deviance to expected log predictive density. The fused posterior combines samples from each modality's posterior proportionally: drawing $\lfloor w_i N_{\text{total}} \rfloor$ samples from modality i's posterior, where N_{total} is the target sample size and $\sum_i w_i = 1$. This approach represents standard ensemble learning where model evidence determines contribution.

Across all scenarios (Figs. S20–S21), BMA maintains near-nominal coverage with competitive interval widths. Under misspecification (Experiments B–D), BMA performs similarly to Fixed- γ (CV) since both rely on hold-out predictive performance, though BMA's evidence-based weighting proves slightly less adaptive than Dirichlet- γ 's learned trust allocation. In the Base clean scenario, BMA achieves comparable RMSE to other tempered methods, demonstrating that model averaging provides robust fusion when modalities are well-specified.

Experiment G: CI (Covariance Intersection). CI provides conservative fusion for correlated estimates with unknown correlation structure (Julier and Uhlmann, 2007). We fit single-modality models and approximate each posterior as Gaussian: $p_i(Y) \approx \mathcal{N}(Y \mid \mu_i, \sigma_i^2)$ using the posterior mean and variance. CI then fuses via the optimal weights $\omega_i \propto 1/\sigma_i^2$ (minimizing the trace of the fused covariance), yielding fused precision $\lambda_{\text{CI}} = \sum_i \omega_i/\sigma_i^2$ and mean $\mu_{\text{CI}} = \lambda_{\text{CI}}^{-1} \sum_i (\omega_i \mu_i/\sigma_i^2)$ where $\sum_i \omega_i = 1$. The fused posterior is $\mathcal{N}(\mu_{\text{CI}}, \lambda_{\text{CI}}^{-1})$. This approach guarantees that the fused covariance bounds the true covariance for any correlation structure, making it maximally conservative.

CI achieves nominal or slightly over-nominal coverage across all scenarios (Fig. S20), confirming its conservative nature. However, this conservatism comes at the cost of wider credible intervals compared to Dirichlet- γ , particularly under misspecification (Experiments B–D) where CI cannot selectively down-weight corrupted modalities. In Fig. S21, CI exhibits higher RMSE than Dirichlet- γ for corrupted scenarios since it equally trusts all modalities through inverse-variance weighting rather than adapting to model-data discrepancies. The Gaussian approximation also sacrifices tail behavior and multimodality present in the full posteriors, limiting CI's applicability when posterior distributions are non-Gaussian.

Aggregated numbers. Table S12 lists coverage, width, and RMSE aggregated by method and scenario.

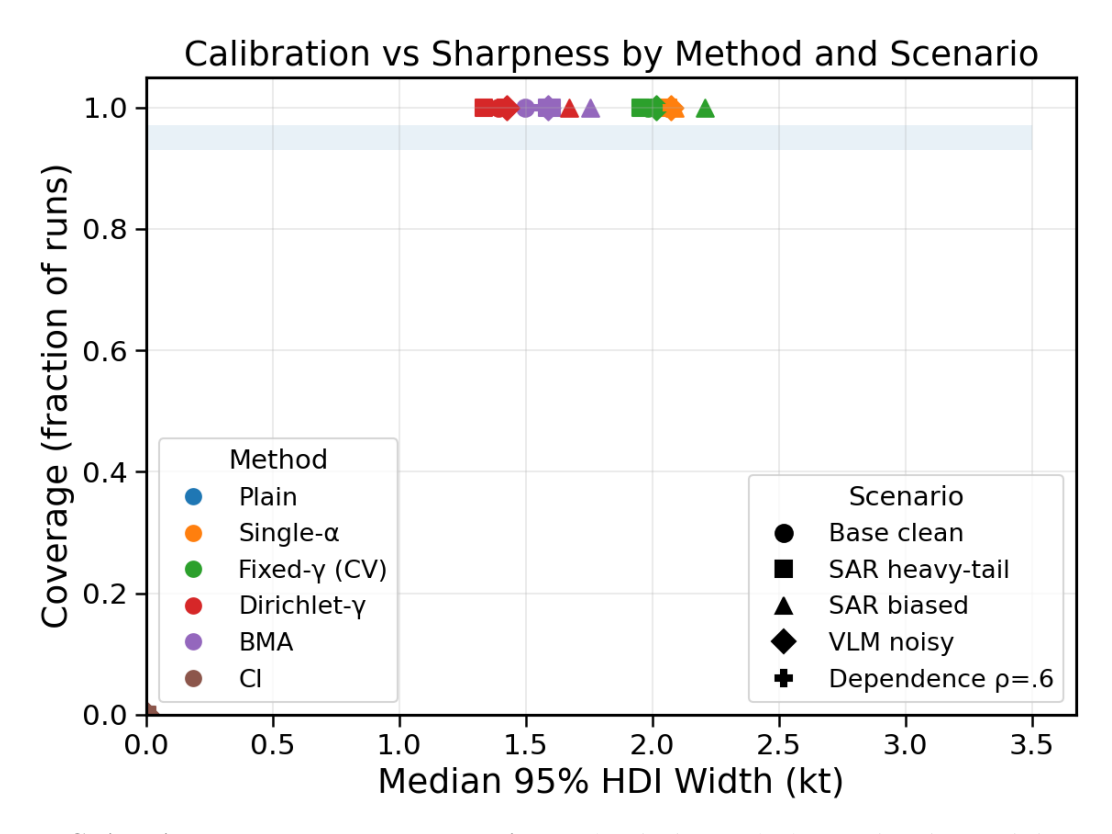


Figure S20: Calibration vs. sharpness across scenarios. Each point is a method–scenario pair: y–axis is coverage of the 95% interval, x–axis is median HDI width.

Table S11: Mechanism summary. Median posterior–mean $\bar{\gamma}$ of the intentionally corrupted modality by scenario shown with "—" indicating that no single corrupted modality.

Scenario	Median γ (corrupted)				
SAR heavy-tail	0.754				
SAR biased	0.762				
VLM noisy	0.240				
Base clean					
Dependence ρ =.6	_				

In Tables S12 and S13, we omit the untempered plain product baseline and covariance intersection methods, which consistently collapsed under mild misspecification (coverage ≈ 0), confirming the need for tempered or adaptive weighting.

S3.3.3 Real-data mechanism check (Beirut)

Subsequently, we compare learned trust to LOO information loss. Let $\bar{\gamma}_i$ be the posterior mean trust of modality i, and $\mathrm{KL}_i = \mathrm{KL}(\pi_{\mathrm{full}}(Y) \parallel \pi_{-i}(Y))$ the divergence when modality i is removed and the model refit. On Beirut we obtain

```
\bar{\gamma} = \{ \text{Seismic } 0.278, \text{ Crater } 0.340, \text{ VLM } 0.219, \text{ SAR } 0.163 \}, \\ \text{KL} = \{ \text{Seismic } 0.130, \text{ Crater } 0.087, \text{ VLM } 0.180, \text{ SAR } 0.342 \}.
```

with a perfect inverse rank alignment (Spearman $\rho = -1.00$), indicating that modalities whose removal causes larger information loss receive smaller learned trust, consistent with the simulated stress tests and the down-weighting of SAR in the fused posterior.

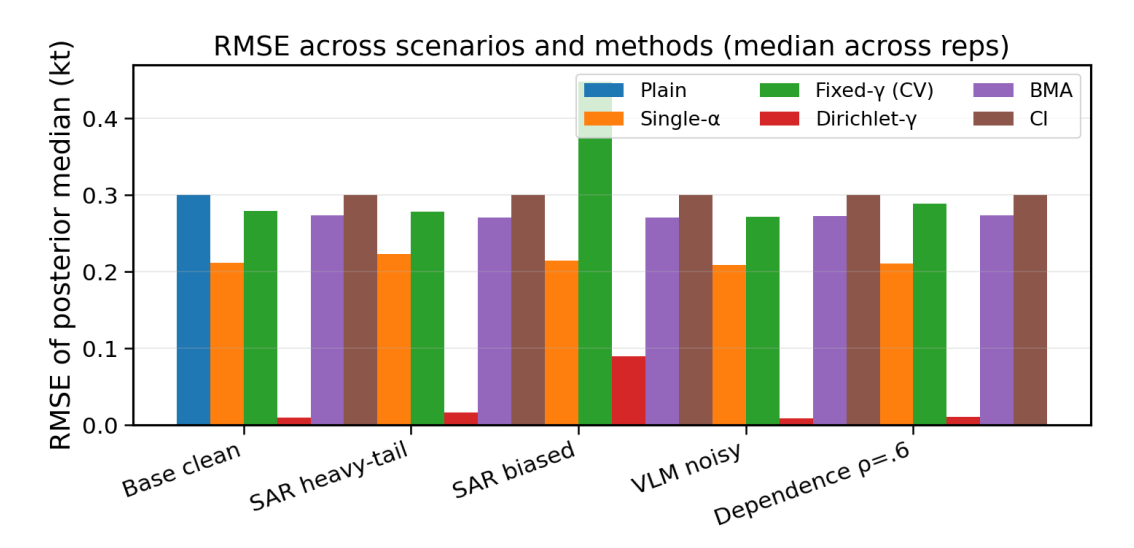


Figure S21: RMSE of posterior median across scenarios. Lower is better.

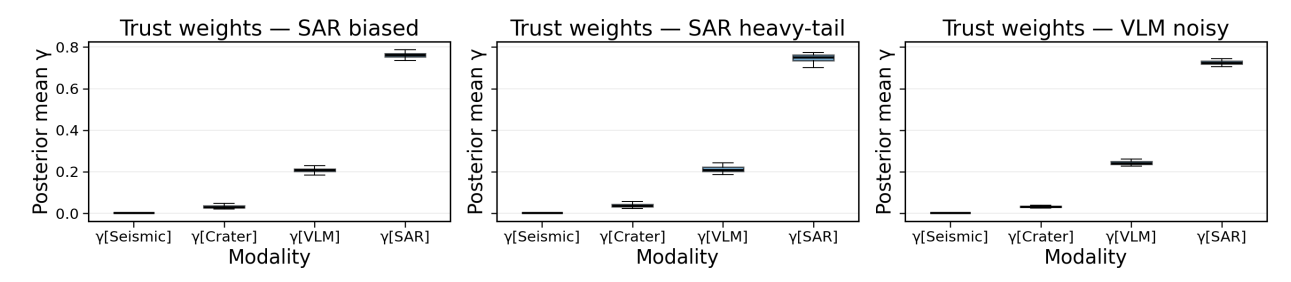


Figure S22: **Mechanism check** (γ). Posterior–mean trust weights by modality under corrupted scenarios. Boxes summarize replicates; lower γ indicates down–weighting of the corrupted modality.

S3.3.4 Sensitivity to Dirichlet Concentration Parameter

The Dirichlet prior on trust weights $\gamma \sim \text{Dirichlet}(\alpha_1, \alpha_2, \alpha_3, \alpha_4)$ requires specification of concentration parameters. Our main analysis uses $\alpha_i = 1$ for all modalities, corresponding to a uniform prior over the simplex. To assess sensitivity to this choice, we last vary the concentration parameter symmetrically ($\alpha_i = \alpha$ for all i) across two orders of magnitude and examine the impact on yield estimates and learned trust weights.

Table S14 summarizes the posterior statistics as α varies from 0.1 to 10. The yield estimates remain remarkably stable: the posterior median ranges from 0.349 to 0.378 kt, a variation of less than 10% across a 100-fold change in α . The 95% HDI width fluctuates modestly between 0.847 and 0.956 kt, maintaining consistent uncertainty quantification. The KL divergence from the baseline ($\alpha = 1$) remains below 0.32 bits for all values, indicating minimal posterior shifts.

Figure S23 illustrates the stability of the yield posterior across different α values. The posterior median and 95% HDI remain nearly constant, demonstrating that our inference is robust to the prior specification. This robustness arises because the data strongly inform the trust weights, overwhelming moderate prior preferences.

Figure S24 reveals how trust weight allocation varies with α . Small values ($\alpha < 1$) favor sparse solutions where crater dominates ($\gamma_{\text{crater}} \approx 0.68$ at $\alpha = 0.1$). As α increases, the weights become more uniform, approaching equal allocation ($\gamma_i \approx 0.25$) for large α . Notably, the relative ranking remains consistent: crater > seismic > VLM > SAR across all values, confirming that data-driven trust relationships persist regardless of prior choice.

This sensitivity analysis confirms that our choice of $\alpha_i = 1$ represents a reasonable default that allows the data to determine trust weights without imposing strong prior beliefs. The stability of yield estimates across different prior specifications strengthens confidence in our multimodal fusion results.

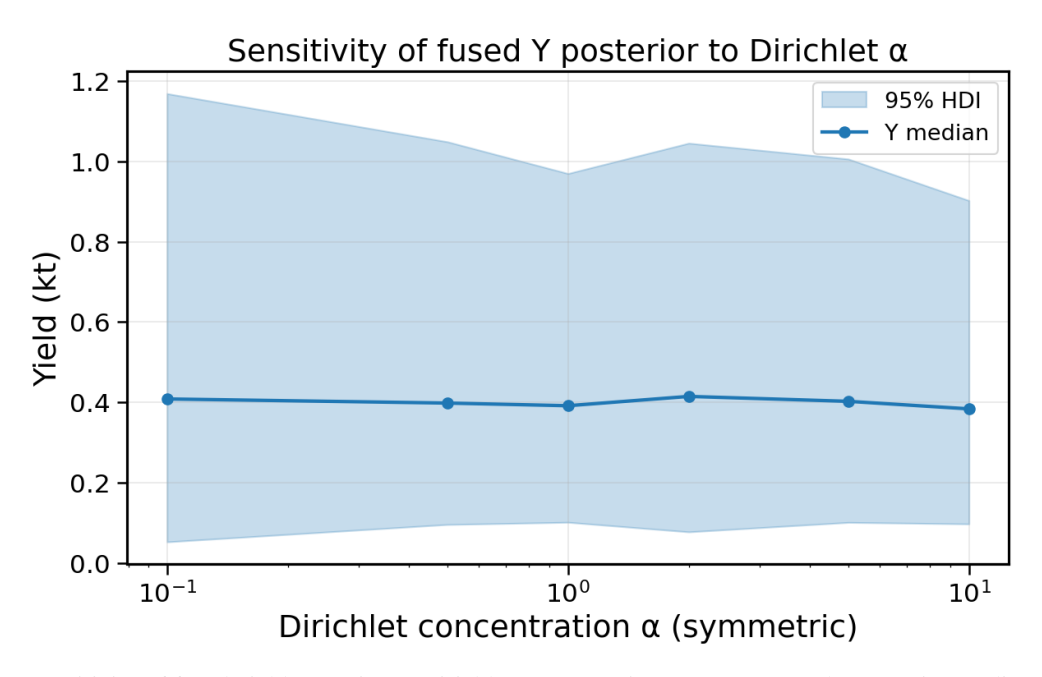


Figure S23: Sensitivity of fused yield posterior to Dirichlet concentration parameter α . The posterior median (blue line) and 95% HDI (shaded region) remain stable across two orders of magnitude variation in α , demonstrating robustness to prior specification.

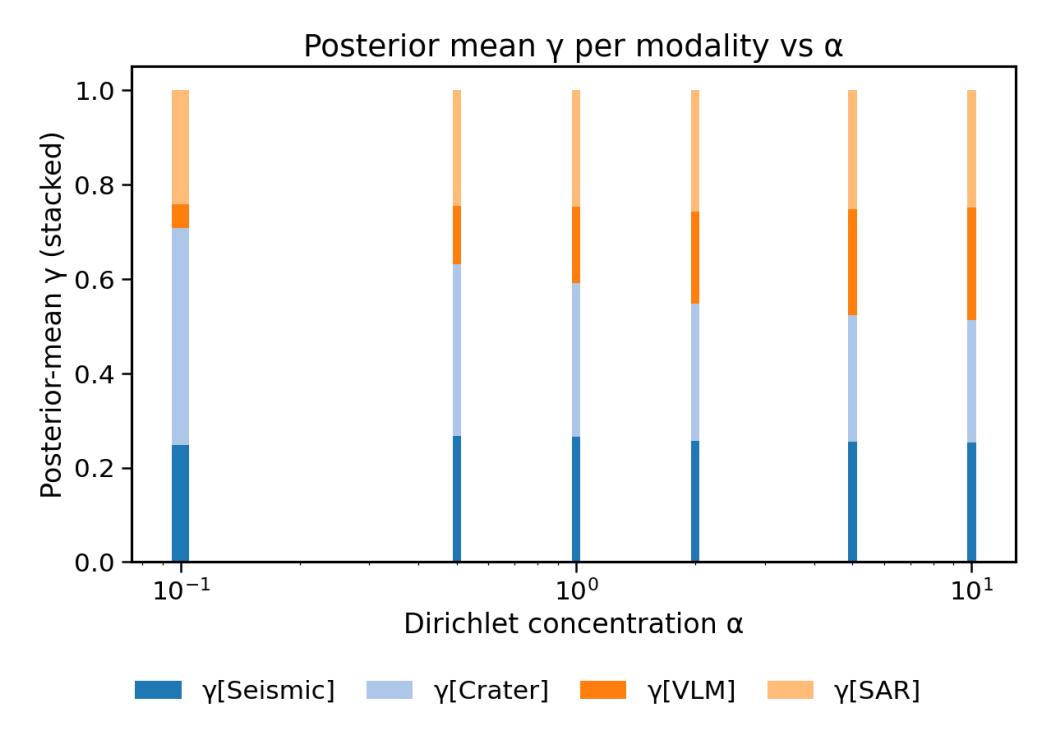


Figure S24: Posterior mean trust weights $\bar{\gamma}_i$ as a function of Dirichlet concentration α . Small α produces sparse weights dominated by crater measurements, while large α encourages more uniform allocation. The relative ranking (crater > seismic > VLM > SAR) remains consistent, indicating robust identification of modality reliability.

Table S12: **Performance by method** \times **scenario.** Coverage (mean), 95% HDI width (median), RMSE (median). Plain product and CI excluded due to implementation failures (coverage \approx 0, width \approx 0).

Scenario	Method	Coverage	Width (kt)	RMSE (kt)
Base clean	Single- α	1.00	2.07	0.191
Base clean	Fixed- γ (CV)	1.00	1.97	0.280
Base clean	BMA	1.00	1.57	0.272
Base clean	Dirichlet- γ	1.00	1.38	0.012
SAR heavy-tail	Single- α	1.00	2.06	0.190
SAR heavy-tail	Fixed- γ (CV)	1.00	1.97	0.276
SAR heavy-tail	BMA	1.00	1.55	0.271
SAR heavy-tail	Dirichlet- γ	1.00	1.35	0.019
SAR biased	Single- α	1.00	2.03	0.183
SAR biased	Fixed- γ (CV)	1.00	2.21	0.447
SAR biased	BMA	1.00	1.71	0.275
SAR biased	Dirichlet- γ	1.00	1.69	0.087
VLM noisy	Single- α	1.00	2.05	0.182
VLM noisy	Fixed- γ (CV)	1.00	1.98	0.273
VLM noisy	BMA	1.00	1.60	0.270
VLM noisy	Dirichlet- γ	1.00	1.43	0.018
Dependence ρ =.6	Single- α	1.00	2.00	0.195
Dependence ρ =.6	Fixed- γ (CV)	1.00	2.04	0.284
Dependence ρ =.6	BMA	1.00	1.59	0.274
Dependence ρ =.6	Dirichlet- γ	1.00	1.40	0.011

Table S13: **Dependence sensitivity** ($\rho = 0.6$). Coverage and median HDI width.

Method	Coverage	Width (kt)		
Single- α	1.00	2.00		
Fixed- γ (CV)	1.00	2.04		
BMA	1.00	1.59		
Dirichlet- γ	1.00	1.40		

Table S14: Sensitivity of yield estimates and trust weights to Dirichlet concentration parameter α

α	Median (kt)	95% HDI (kt)	$\gamma_{ m seismic}$	γ_{crater}	$\gamma_{\rm VLM}$	γ_{SAR}	KL vs α =1
0.1	0.378	[0.096, 0.969]	0.247	0.676	0.056	0.021	0.305
0.5	0.351	[0.068, 0.916]	0.292	0.501	0.136	0.071	0.265
1.0	0.359	[0.101, 1.029]	0.288	0.410	0.183	0.118	0.000
2.0	0.354	[0.087, 1.043]	0.285	0.334	0.223	0.159	0.281
5.0	0.349	[0.072, 0.938]	0.266	0.286	0.240	0.209	0.216
10.0	0.350	[0.059, 0.973]	0.257	0.272	0.242	0.228	0.316